POLITECNICO DI TORINO

MASTER's Degree in Environmental and land Engineering

MASTER's Degree Thesis

Numerical models for convective motion in the atmosphere

Supervisors

Prof Luca BRANDT

Prof. Marica PELANTI

Candidate

Kiarash KAMKAR

July 2026

Numerical models for convective motion in the atmosphere

Kiarash Kamkar

Abstract

Moist atmospheric convection couples turbulent transport, phase change, and buoyancy in ways that remain a leading source of uncertainty in weather and climate prediction. This thesis develops a consistent framework for shallow moist convection that bridges classical Rayleigh–Bénard convection and atmospheric motion with phase change. The model is built on a simplified Baer–Nunziato four-equation diffuse-interface formulation, implemented in the parallel solver FluTAS. Rather than resolving a sharp liquid–gas interface, a mixture description is adopted, in which the two phases share a single velocity, pressure, and temperature field and the condensate is represented through a transported volume fraction, while chemical non-equilibrium is retained to capture condensation and evaporation. Phase change is modelled as a relaxation of the vapour mass fraction towards its saturation value, closed through the Antoine equation, and buoyancy is formulated within the Boussinesq approximation to include thermal, water-vapour, and condensate-loading contributions. The principal novelty of this work is that cloud liquid water is retained as a prognostic field rather than removed instantaneously upon condensation, so that the feedback of suspended condensate on buoyancy is captured directly.

Two simulations are performed under identical numerical and dynamical conditions: a dry reference case, in which no phase change occurs, and a moist case in which condensation, latent heating, and condensate loading are active, so that differences can be attributed unambiguously to phase-change processes. Decomposing the total heat flux into sensible and latent contributions, the analysis characterises the variations in heat flux, Nusselt number, and both vertical and horizontal velocity variance between the two regimes, showing how phase change modifies not only convective heat transport but also the distribution of turbulent kinetic energy between plume motions and near-wall horizontal flow. The results demonstrate that resolving phase change and its buoyancy feedbacks materially alters convective heat transport and flow organisation, while the present framework offers a transparent and reproducible basis for linking laboratory-scale convection theory with moist atmospheric dynamics.

ACKNOWLEDGMENTS

My deepest gratitude goes to my mother, my father, and my brother, whose love and support have been my greatest motivation throughout every step of this journey.

I would also like to express my sincere gratitude to my supervisor, Professor Luca Brandt, for his invaluable guidance, insight, and support throughout this research, which shaped this work at every stage. I am also thankful to Professor Marica Pelanti for her valuable contributions, and to Chang Xu and Hamidreza Zandipour for their collaboration during this work.

Finally, my time at Politecnico di Torino, and particularly within the DIATI Department, has shaped not only this thesis but also the way I think about research itself. My appreciation also goes to all the professors within DIATI with whom I had the privilege of taking courses, as their teaching and guidance contributed greatly to my academic growth.

Table of Contents

List of Figures

List of Tables

Acronyms

ENSO El Ni no–Southern Oscillation.

MJO Madden–Julian Oscillation.

IPCC Intergovernmental Panel on Climate Change.

MCS Mesoscale Convective System.

GCM General Circulation Model.

RH Relative Humidity.

DNS Direct Numerical Simulation.

LES Large-Eddy Simulation.

CRM Cloud-Resolving Model.

RB Rayleigh–B'enard.

OB Oberbeck–Boussinesq.

BN Baer–Nunziato.

FT Front Tracking.

VOF Volume-of-Fluid.

LS Level-Set.

PF Phase-Field.

FA Fast Autoconversion.

FARE	Fast Autoconversion with Rain Evaporation.
Ra	Rayleigh number.
Pr	Prandtl number.
Re	Reynolds number.
Nu	Nusselt number.
Da	Damk"ohler number.
St	Stefan number.
Sc	Schmidt number.
Pr_t	turbulent Prandtl number.
Sc_t	turbulent Schmidt number.

Chapter 1

Introduction and Background

1.1 Atmospheric Convection

Atmospheric convection consists of buoyancy-driven vertical motions, in which warm, less dense air parcels rise and cooler, denser air parcels sink [1]. Unlike diffusive processes, which transfer properties slowly and primarily over local scales, convective motions provide a rapid and strongly non-local mechanism for transporting heat, moisture, momentum, and mass from the surface to the free troposphere on timescales of minutes [2]. Through its coupling with phase changes of water and the associated latent heat release, moist convection plays a central role in shaping weather systems and coupling processes across a wide range of spatial and temporal scales [3].

In the atmosphere, this coupling between vertical motion and phase change manifests as shallow cumulus and deep cumulonimbus clouds (fig. 1.1), which contribute to tropical and subtropical storms as well as mid-latitude weather systems [4]. Individual convective clouds are relatively small, typically spanning a few kilometers to several tens of kilometers. Nevertheless, convection rarely occurs in isolation. Groups of convective cells can interact through their associated circulations, moisture transport, and precipitation processes, leading to the formation of organized mesoscale convective systems (MCSs) that may cover hundreds of kilometers [2]. An important mechanism in this organization process is the formation of cold pools, which are regions of relatively cool and dense air generated by evaporative cooling beneath precipitating clouds. As cold pools spread along the surface, they can lift warm and moist environmental air at their leading edges, triggering new convective cells and promoting the growth and maintenance of larger convective systems. These systems contain multiple clouds embedded within a common circulation and are responsible for a large fraction of tropical rainfall. Through their collective organization and interaction, MCSs influence atmospheric dynamics on progressively larger scales and are regarded as the building blocks of planetary-scale phenomena such as the Madden–Julian Oscillation (MJO), which extends over thousands of kilometers [5].

The latent heat released during condensation and other phase transitions within clouds is, in aggregate, a major heating term for the atmosphere, and convective heating directly drives large-scale atmospheric circulations such as the Hadley circu-

Figure 1.1: Cumulonimbus and Cumulus Cloud Structure.

lation [6, 7], the Walker circulation [8], the El Niño–Southern Oscillation (ENSO) [9], and the MJO [10], as well as extreme weather systems such as tropical cyclones [11]. Beyond this direct heating effect, atmospheric convection is closely connected to cloud–radiation feedback [12, 13], surface flux feedback [14, 15], and chemical transport [16, 17], and it plays a crucial role in global climate change [18]. Both the present climate and its response to anthropogenic forcing depend sensitively on moist convection and its interaction with radiation, large-scale circulation, and surface processes, including surface heat, moisture, and momentum fluxes across the land–atmosphere and ocean–atmosphere interfaces [19]. Consequently, atmospheric convection is one of the leading sources of uncertainty in climate sensitivity estimates and can explain a significant fraction of the spread among more than 40 IPCC-class climate models [20, 21, 22, 23].

Despite decades of research, a comprehensive theoretical framework that consistently links small-scale convective dynamics to large-scale atmospheric variability remains incomplete. The fundamental difficulty arises because moist convection couples turbulent motions, phase transitions, and large-scale dynamics across interacting scales, for which no exact closure exists. Convection is inherently nonlinear and operates on scales much smaller than those resolved by large-scale models; because of this, errors in its representation can rapidly degrade forecast skill. This challenge is particularly acute in the tropics, where convection dominates weather variability and must be properly represented both in mesoscale models for severe storms and tropical cyclones and in climate models that simulate large-scale modes such as the MJO and ENSO [24]. Consequently, despite the importance of tropical convection, its numerical simulation remains a major challenge [25, 26], and improving the modeling of moist convection is essential to advance the prediction of weather and climate.

This thesis focuses on the physical mechanisms governing moist atmospheric convection, with particular emphasis on phase-change processes. These processes belong to the class of so-called fast physics, which includes turbulence, cloud formation, and cloud microphysics. Because their characteristic scales are much smaller than the grid spacing of weather prediction models and General Circulation Models

(GCMs), they cannot be resolved explicitly and must instead be represented through parameterization schemes. Understanding the underlying dynamics of these processes is therefore essential for improving their representation in atmospheric models.

1.2 Dry convection

Dry convection refers to buoyancy-driven motion that occurs in the absence of water-phase changes. In atmospheric applications, dry air is commonly approximated as an ideal mixture composed primarily of nitrogen (N_2), oxygen (O_2), and argon (Ar), with number fractions of approximately 0.7809, 0.2095, and 0.0093, respectively [19]. In this simplified framework the composition is fixed and temperature differences alone generate the density variations that drive the flow: warm, less dense air rises and cooler, denser air sinks. Because it excludes condensation, evaporation, and latent heat release, dry convection provides the reference case in which buoyancy is controlled only by temperature, and it serves as the baseline against which the moist processes discussed in Section 1.4 are understood.

When an air parcel rises in the atmosphere, it moves into regions of lower pressure and expands. This expansion requires energy, and if no heat is exchanged with the surroundings (an adiabatic process) that energy is drawn from the parcel's own internal energy, so its temperature falls. Starting from the first law of thermodynamics,

$$dQ = c_p\, dT - \alpha\, dp, \tag{1.1}$$

where dQ is the heat added to the parcel (zero for an adiabatic process), $c_p = 1005\ \mathrm{J\,kg^{-1}\,K^{-1}}$ is the specific heat at constant pressure, $\alpha = 1/\rho$ is the specific volume, and combining it with hydrostatic balance, $dp/dz = -\rho g$, gives the rate at which a dry parcel cools with height, the *dry adiabatic lapse rate*,

$$\Gamma_d \equiv -\frac{\partial T}{\partial z} = \frac{g}{c_p} \approx 9.8\ \mathrm{K\,km^{-1}}. \tag{1.2}$$

This means a dry parcel cools by roughly $1\,^\circ\mathrm{C}$ for every 100 m of ascent. Physically, this lapse rate corresponds to the conversion of internal energy into gravitational potential energy during adiabatic ascent: the decrease in specific enthalpy c_pT with height is exactly balanced by the increase in gravitational potential energy gz. It is the temperature gradient a dry parcel follows during adiabatic vertical motion.

To compare a parcel with its environment independently of these adiabatic pressure effects, it is convenient to use the *potential temperature* θ, defined as the temperature a parcel would have if brought adiabatically to a reference pressure p_0,

$$\theta = T\left(\frac{p_0}{p}\right)^{R/c_p}, \tag{1.3}$$

where $R = 287\ \mathrm{J\,kg^{-1}\,K^{-1}}$ is the specific gas constant for dry air. Its key property is that it is conserved during adiabatic parcel motion, so that surfaces of constant θ

coincide with isentropes. This makes θ the natural variable for describing atmospheric stability, since a displaced parcel carries its potential temperature unchanged while the environmental profile $\theta_0(z)$ varies with height.

Vertical motion arises when a parcel's density differs from that of its environment. For the small density perturbations typical of the troposphere, and choosing a reference state in which pressure perturbations contribute negligibly to density, the buoyancy reduces to

$$b \approx -g\frac{\rho'}{\rho_0} \approx g\frac{T'}{T_0} \approx g\frac{\theta'}{\theta_0}, \tag{1.4}$$

where the sign change follows from the ideal gas law at constant pressure, $\rho'/\rho_0 = -T'/T_0$. Buoyancy is therefore proportional to the potential-temperature perturbation: a parcel warmer than its surroundings is less dense and accelerates upward [19, 27]. Potential temperature is preferred over temperature here because it removes the adiabatic pressure effect and is conserved during vertical motion, giving a cleaner measure of the parcel's thermodynamic state. This is the same buoyancy–temperature coupling that, in the Boussinesq form $b = g\beta T'$ used for the dry reference case in this work, drives the flow between the heated and cooled plates.

The sign of the environmental gradient $\partial_z\theta_0$ determines whether such displacements grow or decay, giving three cases:

- **Stable** ($\partial_z\theta_0 > 0$): a displaced parcel becomes denser than its new surroundings and returns toward its original level; perturbations are suppressed.
- **Neutral** ($\partial_z\theta_0 = 0$): the parcel matches its environment and feels no net buoyancy. The environmental temperature then decreases with height at exactly the dry adiabatic lapse rate Γ_d.
- **Unstable** ($\partial_z\theta_0 < 0$): a displaced parcel remains warmer and lighter than its surroundings and accelerates away from its original position, so convective motions develop and grow.

When the stratification is unstable, the resulting convection transports warm parcels upward and cold parcels downward, mixing potential temperature across the layer. The flow acts to remove the instability, driving the profile toward a non-decreasing $\theta_0(z)$. In many dry convective regimes, this process produces an approximately well-mixed layer with $\partial_z\theta_0 \approx 0$, corresponding to neutral stratification and the establishment of the dry adiabatic lapse rate.

In the present work, the dry reference case lies within this unstable regime and serves as the baseline against which the effects of moisture and phase changes are assessed. To study the fundamental mechanisms of buoyancy-driven convection in a controlled setting, an idealized Rayleigh–Bénard framework is adopted, in which the lower boundary is maintained at a higher temperature than the upper boundary. The resulting thermal instability generates convective motions driven solely by temperature-induced density differences. The Rayleigh–Bénard configuration and its governing dimensionless parameters, including the Rayleigh number, are introduced in Section 1.4.

Finally, it is worth noting that "dry" convection does not imply the absence of water vapour. The air may still contain water vapour, but it remains unsaturated and therefore does not undergo condensation. As a result, the vapour mixing ratio is approximately conserved during adiabatic parcel displacements. It is this absence of phase change, rather than the absence of water itself, that distinguishes dry convection from moist convection. In the atmosphere, however, rising air parcels frequently reach saturation, allowing condensation and evaporation to occur. These phase changes release or absorb latent heat, modify the buoyancy budget, and introduce additional thermodynamic feedbacks, leading to the moist convective processes discussed in the next section.

1.3 Moist convection

Whereas dry convection is governed solely by temperature-induced density differences, moist convection introduces additional thermodynamic feedbacks through phase changes of water. It plays a central role in shaping planetary atmospheres, driving cloud formation, precipitation, and large-scale circulation patterns [28]. As moist air rises and cools, water vapour may condense into cloud droplets, releasing latent heat that enhances buoyancy and strengthens vertical motions. Clouds therefore represent one of the most visible manifestations of moist convection in the atmosphere. Even basic features, such as the vertical distributions of temperature and water vapour in a moist convecting atmosphere, continue to pose major scientific challenges, and despite decades of research clouds remain among the dominant sources of uncertainty in the accurate projection of future climate states.

To a good approximation, both dry air and water vapour may be treated as ideal gases under atmospheric conditions. Water vapour plays a crucial role because it can condense into cloud droplets, which then enlarge and eventually fall as precipitation. It is often inconvenient to describe atmospheric moisture using water-vapour density ρ_v or vapour pressure e, because these quantities are not conserved and change when air is compressed or expanded. A more useful measure is the *mixing ratio* w, which remains constant as long as no condensation or evaporation occurs. It is defined as

$$w = \frac{M_v}{M_d} = \frac{\rho_v}{\rho_d}, \tag{1.5}$$

where M_v is the mass of water vapour and M_d the mass of dry air. Because dry air usually dominates, w is often expressed in grams of vapour per kilogram of dry air (for example, $w \approx 20\ \mathrm{g\,kg^{-1}}$ in warm tropical air). The term humidity refers to the concentration of water vapour present in the atmosphere [29]. A related quantity is the *specific humidity* q, defined by

$$q = \frac{M_v}{M_d + M_v} = \frac{\rho_v}{\rho_d + \rho_v}, \tag{1.6}$$

which represents the mass of water vapour per total mass of moist air. In most atmospheric conditions, the mass of water vapour constitutes only a very small fraction of the total air mass, generally not exceeding one to two percent [30].

A wet lower surface provides a continuous moisture source. When water vapour condenses, latent heat is released, which enhances convection. Condensation begins when the specific humidity of an air parcel reaches the saturation specific humidity corresponding to its temperature. A convenient measure of how close a parcel is to saturation is the *relative humidity*, defined as

$$r = \frac{q}{q_s(T)}, \tag{1.7}$$

where q is the specific humidity and $q_s(T)$ is the saturation value at temperature T. Condensation occurs when an air parcel reaches saturation ($r = 1$) during ascent and cooling. Conversely, when moist air descends into a warmer and unsaturated environment ($r < 1$), liquid water evaporates due to the increase in saturation specific humidity. This continuous cycle of condensation and evaporation plays a key role in moist convection dynamics.

As a moist air parcel rises, it expands and cools approximately at the dry adiabatic lapse rate. Because the saturation specific humidity decreases rapidly with temperature, the relative humidity of the parcel increases during ascent. When the parcel reaches saturation ($r = 1$), further cooling causes part of the water vapour to condense into liquid droplets, leading to cloud formation. The level at which saturation is first achieved is commonly referred to as the lifting condensation level (LCL).

The condensation process releases latent heat into the surrounding air parcel. This release of energy partially offsets the cooling associated with adiabatic expansion, allowing the parcel to remain warmer and less dense than it would in dry convection. As a result, condensation enhances the parcel buoyancy and can substantially strengthen vertical motions. Latent heating increases the parcel temperature and therefore reduces its density relative to the environment, producing additional positive buoyancy beyond that associated with dry convection through the same temperature–buoyancy relation, $b \approx g\,\theta'/\theta_0$, established in Section 1.2.

The saturation specific humidity, q_s, can be approximated from the Clausius–Clapeyron relation for an ideal gas, assuming that the latent heat of condensation L is constant. The saturation vapour pressure, e_s, is given by [31]

$$e_s = e_0 \exp\left[\frac{L}{R_v}\left(\frac{1}{T_0} - \frac{1}{T}\right)\right], \tag{1.8}$$

where e_0 is a reference saturation vapour pressure at temperature T_0, R_v is the specific gas constant for water vapour, and T is the absolute temperature. The latent heat can be considered a function of temperature and may be approximated as

$$L(T) = L_0 - (c - c_{pv})(T - T_0), \tag{1.9}$$

where $L_0 = L(T_0)$ is the latent heat at a reference temperature T_0, and c and c_{pv} denote the specific heat capacities of liquid water and water vapour, respectively.

The exponential dependence of saturation vapour pressure on temperature implies that warm air can contain substantially more water vapour than cold air. Consequently, a rising warm and humid parcel can release large amounts of latent heat once condensation begins. This strong temperature dependence is one of the fundamental reasons why moist convection differs so markedly from dry convection, and why it is capable of producing intense clouds, thunderstorms, and deep convective systems.

Substituting the temperature-dependent latent heat into the Clausius–Clapeyron relation allows for a more accurate representation of the saturation vapour pressure $e_s(T)$ compared to the assumption of constant latent heat. The specific heat capacities exhibit a weak dependence on temperature and pressure. In particular, the specific heat of water vapour at constant pressure, c_{pv}, increases slightly with temperature (approximately 2% between $-30\,°\mathrm{C}$ and $+30\,°\mathrm{C}$) and can be reasonably approximated as $c_{pv} \approx 1870\ \mathrm{J\,kg^{-1}\,K^{-1}}$. Similarly, the specific heat of liquid water can be taken as $c \approx 4187\ \mathrm{J\,kg^{-1}\,K^{-1}}$ for temperatures above $0\,°\mathrm{C}$, with a modest increase (up to about 8%) at lower temperatures [32].

Table 1.1 presents standard reference values of the saturation vapour pressures over water (e_w) and ice (e_i) over the temperature range $-40\,°\mathrm{C}$ to $+40\,°\mathrm{C}$. Also included are the corresponding latent heats of vaporization (L) and sublimation (L_s).

Table 1.1: Saturation vapour pressures over water (e_w) and ice (e_i), and latent heats.

T (°C)	e_w (Pa)	e_i (Pa)	L_{latent} ($\mathrm{J\,g^{-1}}$)	$L_{s,\mathrm{latent}}$ ($\mathrm{J\,g^{-1}}$)
-40	19.05	12.85	2603	2839
-35	31.54	22.36	2589	2839
-30	51.06	38.02	2575	2839
-25	80.90	63.30	2562	2839
-20	125.63	103.28	2549	2838
-15	191.44	165.32	2537	2838
-10	286.57	259.92	2525	2837
-5	421.84	401.78	2513	2837
0	611.21	611.15	2501	2834
5	872.47	–	2489	–
10	1227.94	–	2477	–
15	1705.32	–	2466	–
20	2338.54	–	2453	–
25	3168.74	–	2442	–
30	4245.20	–	2430	–
35	5626.45	–	2418	–
40	7381.27	–	2406	–

The vapour pressure values in this table are obtained by integrating the Clausius–Clapeyron equation, accounting for the temperature dependence of both latent heat and specific heat capacities. The values reported in Table 1.1 illustrate two important features. First, the saturation vapour pressure increases rapidly with temperature, indicating that warmer air masses can store significantly larger amounts of water vapour. Second, although the latent heat varies with temperature, it remains of the order of $2.5 \times 10^6\,\mathrm{J\,kg^{-1}}$, demonstrating that condensation represents a substantial energy source capable of strongly modifying atmospheric buoyancy. This reference value is also the latent heat adopted in the simulations of this thesis.

Although the Clausius–Clapeyron relation provides the thermodynamic foundation for the temperature dependence of saturation vapour pressure, several empirical approximations are commonly used in atmospheric applications. One of the most widely used is the formulation proposed by Bolton (1980). Bolton (1980) [33] showed that the saturation vapour pressure over liquid water can be accurately approximated (within 0.1%) over the temperature range $-30\,^\circ\mathrm{C} \leq T \leq 35\,^\circ\mathrm{C}$ by the empirical relation

$$e_s(T) = 6.112 \exp\left(\frac{17.67\,T}{T + 243.5}\right), \tag{1.10}$$

where e_s is in millibars (mb) and T is the temperature in degrees Celsius. This empirical formulation is widely used in atmospheric modelling due to its simplicity and high accuracy.

The specific humidity can also be expressed as a function of the water vapour pressure [34]. It is defined as

$$q_v = \frac{m_v}{m} = \frac{\rho_v}{\rho_d + \rho_v} = \frac{e/(R_v T)}{(p-e)/(R_d T) + e/(R_v T)} = \frac{\epsilon e}{p - e + \epsilon e} \approx \frac{\epsilon e}{p}, \tag{1.11}$$

where e is the water vapour pressure, p is the total pressure, R_v and R_d are the specific gas constants for water vapour and dry air, respectively, and $\epsilon = R_d/R_v$. Similarly, the saturation specific humidity can be expressed in terms of the saturation vapour pressure as

$$q_s \approx \frac{\epsilon e_s}{p}. \tag{1.12}$$

Because condensation releases latent heat, saturated air parcels cool more slowly during ascent than dry parcels. Above the LCL, the resulting temperature decrease with height is known as the *moist adiabatic lapse rate*, which typically ranges between approximately 4 and 7 $\mathrm{K\,km^{-1}}$ depending on temperature and moisture content. This reduced cooling rate, compared with the dry adiabatic lapse rate $\Gamma_d \approx 9.8\ \mathrm{K\,km^{-1}}$ introduced in Section 1.2, allows saturated parcels to maintain positive buoyancy over greater depths of the atmosphere and is one of the principal mechanisms responsible for deep convective cloud development.

In this work, however, the saturation vapour pressure is evaluated using the Antoine equation, which will be introduced and discussed in Chapter 2.

1.4 Rayleigh–Bénard convection

Many turbulent flows are driven and sustained by temperature differences, such as convection within stars and planets [35, 36], atmospheric motion [19, 37], and oceanic circulation [38]. The study of convection in the history of science can be traced back to the study of buoyancy by Archimedes. This principle states that a fluid parcel experiences an upward force equal to the weight of the fluid it displaces. At the end of the nineteenth century, the study of convection advanced through the laboratory experiments of Henri Bénard and the theoretical analysis of Lord Rayleigh. Rayleigh demonstrated that a fluid layer heated from below becomes convectively unstable once a critical Rayleigh number is exceeded, leading to the formation of regular convection cells instead of pure thermal conduction [39].

A canonical model for studying buoyancy-driven convection is Rayleigh–Bénard convection (RBC) [40]. In this setup, a fluid layer of height H is heated from below and cooled from above. The top and bottom boundaries are kept at constant temperatures, T_{top} at $z = H$ and T_{bottom} at $z = 0$, such that $\Delta T = T_{\text{bottom}} - T_{\text{top}} > 0$ (see fig. 1.2). Alternatively, a constant heat flux can be imposed at the boundaries by fixing the temperature gradient dT/dz. When a fluid parcel becomes warmer, it expands and its density decreases. In the presence of gravity, this leads to motion: the lighter, warm fluid rises, while the heavier, cold fluid sinks. As a result, convection develops when warm fluid is below cold fluid. In most cases the turbulent convective motion is coupled to other physical processes such as radiative transfer, phase changes, and chemical reactions.

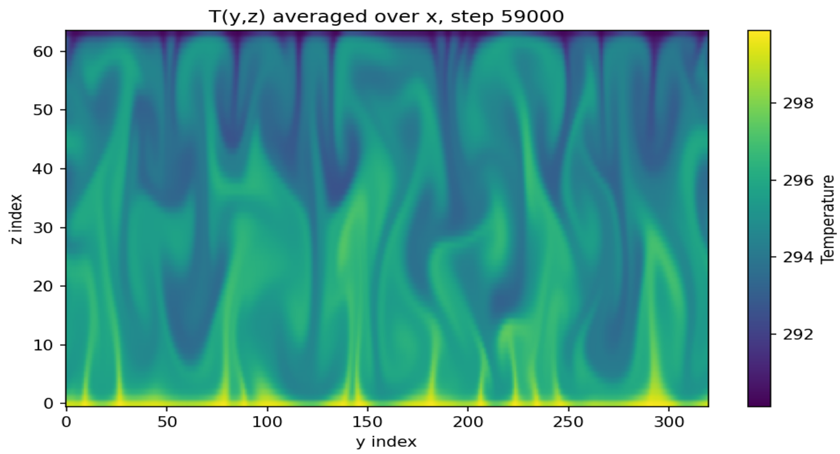

Figure 1.2: Direct numerical simulation (DNS) of dry RB convection at $\mathrm{Ra} = 10^7$.

A fluid parcel will rise when the buoyancy force is strong enough to overcome viscous drag and thermal diffusion. This behaviour can be described using two dimensionless parameters: the Rayleigh number Ra and the Prandtl number Pr, defined as

$$Ra = \frac{g\beta\Delta T H^3}{\nu\kappa}, \qquad Pr = \frac{\nu}{\kappa}, \qquad \Gamma = \frac{L}{H}. \tag{1.13}$$

Here, Γ is the aspect ratio, where L is a characteristic horizontal length scale (for example, the diameter of a convection cell) and H is the domain height. The parameter g denotes gravitational acceleration and β is the thermal expansion coefficient.

The Rayleigh number Ra measures the balance between buoyancy forces that drive the flow and the effects of viscosity and thermal diffusion that resist motion. The Prandtl number Pr compares the relative importance of momentum diffusion (through the kinematic viscosity ν) to thermal diffusion (through the thermal diffusivity κ). Table 1.2 shows typical examples of turbulent convection and provides estimates of the corresponding Rayleigh and Prandtl numbers, together with the characteristic vertical scale H and the aspect ratio $\Gamma = L/H$.

Table 1.2: Examples of convection Rayleigh and Prandtl numbers,

Flow type	Ra	Pr	H	Γ
Deep oceanic convection [41]	10^{24}–10^{27}	7	1–4 km	10^2–10^3
Shallow moist convection [42]	10^{18}	0.7	2 km	10^2
Deep moist convection [31]	10^{22}	0.7	10 km	10

In Rayleigh–Bénard convection, turbulent transport of heat and momentum is mainly governed by near-wall dynamics. The presence of two rigid, impermeable boundaries leads to the formation of thermal and velocity boundary layers, within which coherent turbulent structures, such as plumes and streaks, play a dominant role in transferring heat and momentum across the domain [43, 44].

As the Rayleigh number increases, buoyancy-driven motions become stronger, leading to increasingly turbulent flow. In this regime, transport processes are dominated by turbulent mixing rather than molecular diffusion and viscous dissipation [31]. In particular, large-scale turbulent structures, such as rising and falling plumes, play a central role in transporting heat across the domain. These energetic motions enhance mixing efficiency and effectively redistribute temperature over large distances. While viscosity and thermal diffusivity continue to act at small scales, their relative importance diminishes compared to the large-scale turbulent eddies responsible for heat transport. Consequently, in the ultimate regime at very high Rayleigh numbers, the Nusselt number becomes largely independent of these molecular properties, reflecting a transition from diffusion-controlled to turbulence-controlled transport.

The Rayleigh–Bénard setup can be considered a simplified representation of atmospheric convection and can be used to study moisture effects and cloud-formation feedback mechanisms [45]. The key distinction between atmospheric convection and RB convection lies in the presence of phase transitions in the atmosphere. In atmospheric systems, water evaporates from the Earth's surface, rises with buoyant air parcels, and condenses at higher altitudes. This phase-change process releases latent heat, which reduces the effective adiabatic lapse rate compared to dry convection. Furthermore, clouds formed from suspended condensed water droplets significantly influence the radiative properties of the atmosphere by modifying the albedo and, consequently, the overall energy budget [46, 47]. A deeper physical understanding of cloud feedbacks can be achieved by reducing system complexity and isolating the relevant processes in order to quantify their individual contributions and impacts. In this context, extensions of the classical (dry) Rayleigh–Bénard convection to moist convection are considered within the Oberbeck–Boussinesq (OB) framework.

In steady-state Rayleigh–Bénard convection, heat is transported by turbulent thermal convection from the bottom, hot surface to the top, cold surface, leading to a height-independent sensible heat flux. When water vapour is present and cloud formation occurs, there is also an additional latent heat flux. Heat transport in cloudy Rayleigh–Bénard convection depends on the turbulent flow as well as the microphysical state of the clouds: specifically, whether substantial supersaturations exist and whether cloud liquid water is removed through sedimentation and precipitation.

In contrast to dry convection, moist convection requires tracking additional thermodynamic variables, including water vapour and liquid water (and potentially ice). Consequently, the governing equations become more complex than the standard OB formulation. For warm-cloud conditions, the ice phase can be neglected, reducing the system to two components: water vapour and liquid water.

The buoyancy force in atmospheric convection can be expressed in its general form as

$$B(T, w_v, w_l, p) = -g\,\frac{\rho(T, w_v, w_l, p) - \rho_{\mathrm{ref}}}{\rho_{\mathrm{ref}}}, \tag{1.14}$$

where T denotes the (potential) temperature, and w_v, w_l are the mixing ratios of water vapour and liquid water, respectively. This formulation extends the buoyancy term in the momentum equation to account for multiphase effects. In the limit of single-phase (dry) convection, this expression reduces to the classical form

$$B = \beta g (T - T_{\mathrm{ref}}). \tag{1.15}$$

In the absence of precipitation, water vapour and liquid water only interconvert through phase change, so their sum, the total water mixing ratio

$$w_t = w_v + w_l, \tag{1.16}$$

is conserved locally and can be used to simplify the governing equations. When sedimentation of liquid water is included, as in the present work, this local conservation is relaxed: settling transports liquid downward and removes it through the lower boundary as precipitation. Total water is nonetheless conserved in an integral sense, provided the liquid flux leaving the domain is accounted for in the water budget.

1.5 Literature Review of moist convection study

Although more than 180 years have passed since James Pollard Espy first recognized that cumulus clouds are powered by the release of latent heat during condensation [29], many fundamental properties of moist convection are still not fully understood. Convection occurs in the atmosphere in many different contexts, from the planetary boundary layer to storms with high kinematic fluxes that drive convection through the depth of the troposphere; deep precipitating clouds can be organized in different patterns and can propagate over long distances in the atmosphere [4]. The study of moist convection also depends on the environmental conditions, and convective systems can be organized over multiple length scales and with different aspect ratios. For example, in the tropical atmosphere, deep moist convection creates a variety of clouds at different scales; groups of interacting convective cells organize into systems with horizontal extents of order 100 km and lifetimes of 1 h to 1 day, commonly called mesoscale convective systems (MCSs) [48, 4].

To study these processes, a hierarchy of numerical models has been developed, ranging from comprehensive cloud-resolving models to highly idealized Rayleigh–Bénard configurations. Among the idealized moist-convection studies most relevant to the present work are those of Hernandez-Duenas et al. [48], Vallis et al. [31], Zhang et al. [49], and Thomas et al. [50]. A recurring simplification across this hierarchy is the treatment of condensed water: some models remove condensate from the system the moment it forms, while others convert it instantaneously into rain. How condensed water is represented, and which physics is lost under each simplification, is a guiding question of this review and the central motivation for the present work. The review proceeds from comprehensive atmospheric models through simplified moist-convection models to moist Rayleigh–Bénard studies , before identifying the remaining gap and introducing the present study.

Moist atmospheric convection and cloud-resolving models

One class of numerical models used to study convection is cloud-resolving models (CRMs), which attempt to include all relevant physical processes. These comprehensive numerical models employ grid spacings of about 1 km, as opposed to general circulation models (GCMs), which use grid spacings of order 100 km and must therefore parameterize clouds as a subgrid-scale process [48]. In smaller domains with horizontal scales of 100–1000 km, CRMs are able to reproduce both scattered convection and squall-line regimes in response to different background wind shears [51], and they can provide further details that are often unavailable from observational data. Moreover, several studies have shown that the main regimes of convective organization can be reproduced using a 2D configuration (x, z), in which the flow is assumed to be uniform in one horizontal direction (y) [52, 53, 54, 55, 56].

Comprehensive simulations of moist convection, such as atmospheric CRMs, typically use a non-Boussinesq dynamical core, such as the anelastic equations, and include the water phases explicitly: liquid water, water vapour q_v, and ice. In these formulations, liquid water itself is further separated into cloud water q_c, consisting of small droplets suspended in the air, and rain water q_r, consisting of larger droplets that fall relative to the flow.

Many cloud-resolving and convection models employ the anelastic approximation [57, 58, 59, 60]. The motivation for this choice is twofold. First, the anelastic framework accounts for vertical density stratification by assuming a background density that varies with height, $\tilde{\rho}(z)$. A key quantity in these studies is the density scale height, defined as

$$H_\rho = -\tilde{\rho}\left(\frac{d\tilde{\rho}}{dz}\right)^{-1}, \tag{1.17}$$

which represents the characteristic vertical distance over which density changes significantly. In the Earth's atmosphere, this scale is typically of the order of $H_\rho \approx 8\,\mathrm{km}$. Therefore, when the vertical extent of fluid motion is comparable to several kilometres, density variations become important and must be retained, as in the anelastic framework; in contrast, for shallow flows (e.g., laboratory convection or domains of a few hundred metres), density variations are negligible and the Boussinesq approximation is often sufficient. Second, the characteristic time scales of atmospheric motion are governed by buoyancy-driven processes and are much longer than those associated with acoustic waves. For typical atmospheric flows, convective velocities are of order $U \sim 1$–$10\,\mathrm{m\,s^{-1}}$, whereas the speed of sound is $c \sim 340\,\mathrm{m\,s^{-1}}$, leading to a low Mach number $\mathrm{Ma} = U/c \sim 10^{-3}$–$10^{-2}$. This clear separation of time scales implies that compressibility effects associated with acoustic waves are negligible, so that fast acoustic modes can be filtered out and the description focuses on the slower, dynamically relevant processes of convection and stratification. In this sense, the anelastic approximation used in these models may be interpreted as describing a compressible fluid in which sound waves are neglected [57, 58, 59, 60].

In these anelastic formulations, the thermodynamic variables are decomposed into a background state, denoted by $\tilde{\rho}(z)$, $\tilde{p}(z)$, $\tilde{T}(z)$, and $\tilde{\theta}(z)$, and small perturbations associated with fluid motion. The background state is assumed to be in hydrostatic balance, providing a vertically stratified but motionless reference profile. Density variations are treated as small and are retained only in the buoyancy term of the momentum equation, ensuring that their dynamical effect is limited to gravity-driven motions. The resulting governing equations describe the evolution of velocity, mass, temperature, and water phases, while employing simplified representations of cloud microphysics, and retain the essential physical processes of moist convection, such as buoyancy, stratification, and phase change, while significantly reducing the complexity of the full compressible system. As a representative example, the moist anelastic system discussed by Hernandez-Duenas et al. [48] can be written as:

$$\frac{D\mathbf{u}}{Dt} = -\nabla\left(\frac{p'}{\tilde{\rho}(z)}\right) + \mathbf{k}g\left(\frac{\theta - \tilde{\theta}(z)}{\tilde{\theta}(z)} + \epsilon_0(q_v - \tilde{q}_v(z)) - q_c - q_r\right), \tag{1.18}$$

$$\nabla \cdot (\tilde{\rho}(z)\mathbf{u}) = 0, \tag{1.19}$$

$$\frac{D\theta}{Dt} = \frac{L\tilde{\theta}(z)}{c_p\tilde{T}(z)}(C_d - E_r), \tag{1.20}$$

$$\frac{Dq_v}{Dt} = -C_d + E_r, \tag{1.21}$$

$$\frac{Dq_c}{Dt} = C_d - A_r - C_r, \tag{1.22}$$

$$\frac{Dq_r}{Dt} - \frac{1}{\tilde{\rho}(z)}\frac{\partial}{\partial z}\left(\tilde{\rho}(z)V_T q_r\right) = A_r + C_r - E_r. \tag{1.23}$$

In this formulation, $\mathbf{u}(\mathbf{x}, t)$ is the velocity vector with components (u, v, w), $\mathbf{k}$ is the unit vector in the direction of gravity, and the material derivative is defined as $\frac{D}{Dt} = \frac{\partial}{\partial t} + \mathbf{u} \cdot \nabla$. The total thermodynamic variables $\rho(\mathbf{x}, t)$, $p(\mathbf{x}, t)$, $\theta(\mathbf{x}, t)$ and $T(\mathbf{x}, t)$ are decomposed into a background (anelastic) state and a perturbation. For example, $\rho(\mathbf{x}, t) = \tilde{\rho}(z) + \rho'(\mathbf{x}, t)$ with $|\rho'| \ll |\tilde{\rho}|$, and similarly for the other variables; for instance, the water vapour is written as $q_v(\mathbf{x}, t) = \tilde{q}_v(z) + q_v'(\mathbf{x}, t)$. The governing equations of these models are formulated in terms of full prognostic variables such as velocity, potential temperature, and water mixing ratios. However, these variables evolve relative to a prescribed background state, and their deviations from this state effectively represent the perturbations. The background profiles are not solved dynamically but are fixed and enter the equations through buoyancy and thermodynamic terms. Therefore, such models implicitly capture the evolution of perturbations while solving for the full fields.

In these formulations, the source terms represent phase-change and microphysical processes (Figure 1.3), including condensation C_d, evaporation E_r, auto-conversion A_r, and collection C_r; each source requires modelling, typically involving bulk cloud physics [45, 61, 62]. The terms C_d and E_r depend on the saturation specific humidity $q_{vs}(p, T)$ (via the Clausius–Clapeyron relation), which is a function of temperature and pressure [32], and the rain terminal velocity V_T is specified as a function of droplet size.

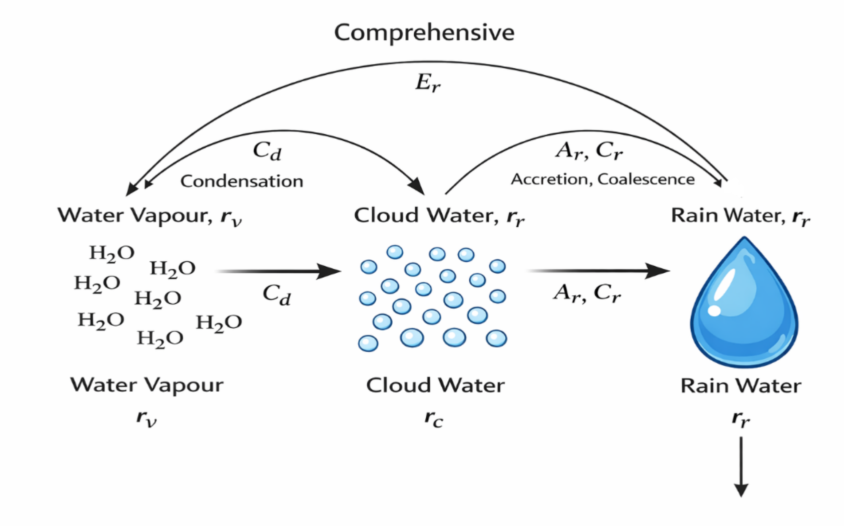

Figure 1.3: Schematic diagrams of cloud physics in numerical models.

The cloud-physics source terms in these models thus depend fundamentally on the saturation water vapour $q_{vs}(p, T)$, which is a function of temperature and pressure only [32]. In CRMs, the saturation water vapour pressure is defined by the Clausius–

Clapeyron relation [31, 48, 32]. However, in some simplified models, the saturation water vapour is approximated as $q_{vs}(z)$, a function of height only.

Simplified moist-convection models

While the level of detail in CRMs is appropriate for weather prediction and for comparison with observations, it may obscure some fundamental aspects of convective dynamics. In particular, certain key features of convection can be reproduced using simplified models with reduced physical complexity. For example, a key distinction between shallow and deep convection is the presence of precipitation-cooled downdrafts in the latter. Deep convection extends over vertical scales comparable to the depth of the troposphere (approximately 10 km), whereas shallow convection is confined to much smaller vertical scales (of order 1 km) and generally does not involve precipitation. Consequently, shallow convection and cloud formation can be described using simplified moist models that focus primarily on water vapour and cloud water [63, 64, 65, 66]. For such simplified models, a reduced form of fast-autoconversion cloud physics is often adopted, in which the autoconversion (A_r) of cloud water q_c to rain water q_r is assumed to occur rapidly.

Several studies have employed simplified frameworks based on the Boussinesq approximation combined with bulk representations of cloud physics [48, 31, 49, 50]. As noted in Section 1.5, the Boussinesq approximation is appropriate when the vertical extent of the flow is small compared with the density scale height H_ρ [60]. Under this assumption, background thermodynamic variables such as density, pressure, and temperature can be treated as constant, while stratification is represented through a linear variation of potential temperature, typically written as $\theta(z) = \theta_0 + Bz$. In this framework, temperature variations are small and influence the dynamics only through the buoyancy term, whereas density is assumed constant elsewhere. This approximation is widely used in studies of shallow convection and laboratory-scale flows, but becomes less accurate for deep atmospheric motions where density variations are significant.

Furthermore, in such simplified models, the cloud microphysics is highly reduced: not only are ice-phase processes neglected, but cloud droplets, once formed, are assumed to grow rapidly and convert into rain droplets. Previous studies have explored simplified models of moist convection with fast autoconversion to better understand the fundamental dynamics of precipitation processes. Early work by Seitter and Kuo [67] investigated two-dimensional simulations of such models, while Emanuel [68] examined the instabilities arising in linear systems incorporating fast autoconversion. Later, Majda [69] applied this approach within a weak-temperature-gradient framework to study the early development of hurricanes. Subsequent studies relaxed this approximation to allow for more realistic dynamics: Sukhatme [70] investigated two-dimensional precipitating stratified turbulence with inertia–gravity waves included, and Deng [71] extended the framework to a three-dimensional Boussinesq model. Their work focused on the interaction between moisture and low-level vertical wind shear, highlighting their combined role in processes such as cyclogenesis. Together, these studies demonstrate that simplified models with fast autoconversion can successfully capture key aspects of moist convective dynamics while remaining computationally tractable.

In particular, Hernandez-Duenas et al. [48] proposed a minimal model that captures the essential features of turbulent moist convection while explicitly including precipitation through a simplified representation in which rainwater falls with a prescribed terminal velocity. Their work introduced simplified Boussinesq systems that include water vapour and rainwater, while neglecting detailed microphysical processes such as droplet size distributions and complex phase-change kinetics. A key simplification in their approach is the assumption of fast autoconversion (FA), whereby cloud water is instantaneously converted into rainwater, eliminating the need to explicitly model cloud liquid water. This reduces their governing equations to a system involving only water vapour and rainwater, while still retaining the essential coupling between thermodynamics and fluid motion.

To further simplify the system and improve robustness, the authors proposed an extended model, referred to as FARE (Fast Autoconversion with Rain Evaporation), in which not only autoconversion but also condensation and evaporation processes are assumed to occur on very fast time scales. In this limit, their microphysical source terms become effectively instantaneous, removing the need for parameterized closures and reducing numerical stiffness. The FARE model is formulated in terms of conserved thermodynamic variables, such as the total water mixing ratio and the rainwater potential temperature, allowing the system to retain key conservation properties while remaining mathematically tractable. An important feature of their formulation is the inclusion of an energy-consistent framework, in which precipitation not only transports energy but also acts as a sink due to the gravitational settling of rain droplets. This effect represents an additional mechanism through which moist processes influence the dynamics of convection. At the same time, their fast-autoconversion assumption means that suspended cloud liquid water is never explicitly represented in their model: condensate is transferred immediately to the rain category, so the residence of liquid water in the flow, and its direct feedback on buoyancy through condensate loading, are not captured. This simplification is shared, in different forms, by several of the idealized models discussed below, and it is precisely the aspect that the present work seeks to relax.

Moist Rayleigh–Bénard convection

In addition to atmospheric models, convection has been extensively studied in the framework of Rayleigh–Bénard (RB) convection, which represents a canonical configuration for buoyancy-driven flows [45, 31, 49, 72, 50]. In this setup, as explained in Section 1.4, a Boussinesq fluid is confined between two horizontal plates maintained at different temperatures, leading to convective motion when the temperature difference exceeds a critical threshold. Despite its simplicity, RB convection captures many fundamental features of convective dynamics, including instability, pattern formation, and the transition to turbulence. As such, it provides a useful idealized framework for understanding key aspects of convective processes and has been widely used as a reference system for both dry and moist convection studies.

A very large body of literature exists on these problems; comprehensive reviews are given by Ahlers, Grossmann and Lohse [73] and Chillà and Schumacher [74]. However, atmospheric convection is much more complex than classical Rayleigh–Bénard convection, and previous studies of moist Rayleigh–Bénard convection have therefore been conducted to better understand atmospheric convection processes. Although condensation is a primary difference between Rayleigh–Bénard and atmospheric convection, other important distinctions exist. Rayleigh–Bénard convection typically considers a dry Boussinesq fluid confined between two plates, where buoyancy is driven solely by diffusive heat fluxes at the boundaries. In contrast, atmospheric convection often involves moisture, occurs in an ideal gas without a rigid upper boundary, and is influenced by radiation, which both heats the fluid near the surface and cools it internally. Radiative cooling introduces an up–down asymmetry in the flow, which can be as important as moisture effects. By cooling the fluid internally, it enhances turbulent mixing and may help reduce the limiting role of molecular diffusion in the boundary layers [75, 76].

In addition to these effects, an important distinction between Rayleigh–Bénard convection and atmospheric convection lies in the role of shear and surface-layer processes. In classical Rayleigh–Bénard convection, turbulence is primarily driven by buoyancy, while shear arises only locally within boundary layers as a consequence of no-slip boundary conditions and convective motions. In this case, the influence of the boundaries is governed by molecular diffusion and viscous effects within thin thermal and velocity boundary layers [31]. In contrast, the atmospheric boundary layer is strongly influenced by imposed shear induced by large-scale winds with specific mean wind profiles and surface roughness, which act as additional sources of turbulence and significantly modify boundary-layer dynamics. As a result, turbulent transport near the surface is more accurately described by similarity theories, such as the Monin–Obukhov framework [77], which relates fluxes of momentum and heat to macroscopic parameters like the friction velocity, the surface roughness length, and the Monin–Obukhov length. Unlike RB convection, this approach does not rely on molecular viscosity or diffusivity, but instead captures the dominant role of turbulent mixing. Therefore, while RB convection provides a fundamental framework for studying buoyancy-driven flows, atmospheric convection requires additional considerations of shear, surface effects, and empirical scaling laws to describe near-surface turbulence.

It should also be mentioned that surface roughness enhances turbulence and heat transfer in both Rayleigh–Bénard convection and the atmospheric boundary layer by modifying near-wall flow structures [72, 74]. In the atmospheric boundary layer in particular, surface roughness plays a crucial role by enhancing velocity gradients near the surface and generating shear-driven turbulence. This increased turbulence promotes mixing of momentum, heat, and moisture, leading to stronger vertical transport and larger surface fluxes [31]. As a result, rougher surfaces are associated with more efficient heat transfer and a more active and deeper boundary layer.

Beyond these physical distinctions, the theoretical and numerical frameworks adopted in each field have also diverged considerably. Theories of atmospheric convection have historically been grounded in plume-based models and quasi-equilibrium frameworks, originating from foundational works such as Scorer & Ludlam [78], Morton, Taylor & Turner [79], and Ludlam [80], and later refined by Emanuel, Neelin & Bretherton [45]. In contrast, Rayleigh–Bénard convection has been approached through statistical turbulence theory and scaling relations [73, 74], with flow behaviour governed by two well-defined dimensionless parameters: the Rayleigh number, which quantifies the ratio of buoyancy-driven to diffusive transport, and the Prandtl number, which characterizes the fluid's thermophysical properties. A fundamental challenge in atmospheric modelling lies in the inability to resolve all relevant scales of motion, since computational resources remain far from sufficient to capture molecular-level viscosity and diffusion, or even individual cloud plumes [81]. To account for unresolved sub-grid turbulence, atmospheric models employ turbulence closure schemes, most notably eddy-viscosity approaches such as the Smagorinsky model [82] and the Mellor & Yamada scheme [83], as well as two-equation k–ε models, which approximate turbulent transport through a modelled turbulent viscosity linked to the turbulent kinetic energy k and its dissipation rate ε. More computationally demanding approaches, such as Large Eddy Simulation (LES), partially resolve the larger energy-carrying eddies while modelling only the smaller sub-grid scales, offering improved accuracy at the cost of greater computational expense [82, 81]. Despite these advances, the Rayleigh and Prandtl numbers — central to laboratory-scale Rayleigh–Bénard theory — play virtually no direct role in most atmospheric convection models, reflecting a fundamental disconnect between the two frameworks. This divergence means that phenomena observed in one modelling context, such as convective aggregation, may not be reproducible in another, raising important questions about whether such behaviours reflect true physical dynamics or are artefacts of specific model configurations [45, 84]. Model intercomparison projects have been developed as a practical response to this reproducibility challenge, allowing results from multiple models to be evaluated side by side [81]. In stark contrast, dry Rayleigh–Bénard convection is governed by its two dimensionless parameters, giving it a clean and controlled mathematical structure in which both the transition to turbulence and key turbulent flow properties are now reliably and reproducibly modelled across independent research groups [73, 74].

Although dry Rayleigh–Bénard convection provides a well-controlled theoretical framework, it is in itself a poor direct model of atmospheric convection, since its simplifications become oversimplifications in an atmospheric context [73]. Nevertheless, a number of studies have sought to bridge this gap. Emanuel [45] opens his treatise on atmospheric convection with a discussion of plumes and the Rayleigh–Bénard problem, explicitly acknowledging the conceptual link between the two systems.

Bretherton [64, 85] examined non-precipitating convection by including liquid water in a fluid confined between two plates, while Spyksma, Bartello & Yau [86] extended this approach using bubble simulations in a triply periodic domain. Pauluis & Schumacher [87] and Schumacher & Pauluis [88] retained liquid water and employed a piecewise-linear equation of state in which buoyancy derivatives depend on whether a parcel is saturated or not. Related problems of two-phase Rayleigh–Bénard convection have also been studied, including boiling flows [89, 90] and mantle convection [91]. Taken together, these studies reflect a growing recognition that moist Rayleigh–Bénard convection occupies a critical intermediate position between idealized dry convection and the full complexity of atmospheric systems.

Vallis et al. [31] introduced the Rainy–Bénard model as an idealized extension of classical Rayleigh–Bénard convection incorporating moist processes in a simplified and transparent manner. In their framework, the standard Boussinesq system is augmented by a prognostic moisture variable, with phase change represented through a simplified Clausius–Clapeyron relation. In their model, condensation acts as a source of buoyancy via latent heat release, while condensate is assumed to precipitate instantaneously and is therefore removed from the system, providing a minimal yet physically meaningful model of moist convection. Their lower boundary is maintained at saturation, fixing the water vapour mixing ratio at its local saturation value and establishing a vertical moisture gradient, since the fluid above is generally unsaturated. Water vapour is transported upward by diffusion and continuously replenished by evaporation at the lower boundary, while rising air that cools to supersaturation undergoes condensation, releasing latent heat and coupling the temperature and moisture fields throughout the domain. An important feature of their model is the existence of a no-motion, or “drizzle”, solution in which the velocity field vanishes identically and transport is governed solely by diffusion and phase change. In this steady state, the upward diffusive moisture flux is exactly balanced by condensation in the bulk, and the momentum equation is satisfied through a pressure balance, so that this stationary solution exists independently of the Rayleigh number. However, for sufficiently large Rayleigh numbers, the drizzle solution becomes unstable, giving rise to buoyancy-driven convection. The existence and subsequent instability of this solution highlight a fundamental distinction between dry and moist convection: phase-change processes introduce thermodynamic mechanisms that can both stabilize and destabilize the flow in ways that have no counterpart in classical dry Rayleigh–Bénard convection. At the same time, the instantaneous removal of condensate means that their Rainy–Bénard model cannot represent the dynamics of suspended cloud water: their formulation contains no condensate loading in the buoyancy, no re-evaporation of falling liquid in subsaturated regions, and no finite-time coupling between the condensate field and the flow.

Additionally, Zhang et al. [49] investigated the mass-transfer properties of water vapour in a moist turbulent natural convection system, motivated by evaporation processes above a heated fluid layer. In their formulation, the system was assumed to be free of condensation nuclei and sufficiently far from the critical point, such that no condensation occurred inside the bulk region of the convection cell. Instead, in their setup, evaporation takes place at the lower boundary and condensation at the upper boundary. Their flow was modelled using the Oberbeck–Boussinesq approximation together with separate advection–diffusion equations for temperature and water vapour concentration. Their governing system introduces buoyancy contributions from both temperature and vapour variations, such that the buoyancy force is proportional to $(\alpha\Delta T + \beta\Delta e)g$, where, in their notation, α is the thermal expansion coefficient, β is the vapour expansion coefficient, ΔT is the imposed temperature difference, and Δe is the vapour-pressure difference across the domain. Based on this formulation, Zhang et al. defined a generalized Grashof number as $Gr = \frac{(\alpha\Delta T+\beta\Delta e)gH^3}{\nu^2}$, which characterizes the combined buoyancy effects generated by thermal and moisture gradients.

The authors further proposed the parameter set $\{Gr, \Lambda, Pr, Sc\}$ as the complete set of control parameters for their two-component convection system. Here, $\Lambda = \frac{\alpha\Delta T}{\beta\Delta e}$ is the buoyancy ratio, representing the relative contribution of thermal buoyancy to vapour-induced buoyancy. They showed that both the sensible heat transfer rate and the moisture transfer rate are primarily controlled by the generalized Grashof number and depend only weakly on the buoyancy ratio.

A limitation of the formulation of Zhang et al. [49] is that latent heating and cooling are not directly coupled to their temperature equation. In their model, the temperature field evolves only through advection and diffusion, while moisture affects the dynamics indirectly through buoyancy. Consequently, important thermodynamic effects associated with phase change, such as evaporative cooling near the lower boundary and condensational heating near the upper region, are not explicitly represented in their temperature evolution.

Thomas et al. [50] extended the Rayleigh–Bénard framework to cloudy convection with explicit phase-change effects and cloud microphysics. Their main objective was to connect the classical fluid-dynamics description of Rayleigh–Bénard convection with atmospheric cloud-physics concepts. In contrast to dry convection, where heat transport is described mainly by the Rayleigh, Prandtl, and Nusselt numbers, cloudy convection involves additional processes such as water-vapour transport, condensation and evaporation, supersaturation, and droplet sedimentation. Therefore, Thomas et al. introduced a non-dimensional formulation of the governing equations and identified the relevant control parameters for cloudy convection, including the Schmidt number, Lewis number, Damköhler number, Stefan number, supersaturation, and Rouse number.

In their formulation, the temperature equation contains an explicit latent-heating term due to condensation and evaporation, while separate equations are solved for water vapour and liquid water. This makes their model more thermodynamically complete than simplified moist convection models in which moisture only affects buoyancy. They showed that the sensible heat flux and latent heat flux can vary with height because phase change locally converts energy between sensible and latent forms. However, by combining the temperature and water-vapour equations, they derived an equivalent heat flux, which remains approximately constant with height at statistical steady state. This flux leads to an equivalent Nusselt number for cloudy convection and is closely related to the atmospheric concepts of equivalent temperature and moist static energy.

Thomas et al. also performed large-eddy simulations of an idealized cloudy Rayleigh–Bénard system, motivated by the Pi Chamber configuration, with different aerosol injection rates. By changing the aerosol concentration, they varied the cloud microphysical state, including the droplet number concentration, liquid water content, supersaturation, sedimentation effects, and the Damköhler number. Their results showed that the individual sensible and latent heat flux profiles depend strongly on the liquid water content and cloud microphysics, whereas the equivalent heat flux is only weakly sensitive to these details and remains nearly conserved across the chamber. A limitation of their work is that their simulations are based on an idealized laboratory-scale cloud-chamber configuration with fixed boundary conditions. Therefore, although their study provides an important bridge between Rayleigh–Bénard convection and atmospheric cloud physics, it does not directly address large-scale atmospheric convection, where additional processes such as large-scale circulation, entrainment, precipitation, radiation, and environmental stratification may become important.

Research gap

Taken together, the studies reviewed above span a hierarchy of idealized moist-convection models, but each simplifies the treatment of condensed water in a different way. In the fast-autoconversion models of Hernandez-Duenas et al. [48], cloud liquid water is eliminated by construction, being converted instantaneously into rain. In the Rainy–Bénard model of Vallis et al. [31], condensate is removed from the system the moment it forms, so that no liquid-water field exists at all. In the formulation of Zhang et al. [49], phase change is confined to the boundaries and latent heating does not enter the temperature equation. The cloud-chamber simulations of Thomas et al. [50] do retain a liquid-water field with detailed microphysics, but in a laboratory-scale configuration tied to aerosol injection and chamber boundary conditions. A gap therefore remains for a moist Rayleigh–Bénard framework in which cloud liquid water is retained as a prognostic field within a controlled, parameter-governed convection setup: one in which condensate persists in the flow for a finite time, is transported and sediments with a prescribed settling velocity, can re-evaporate in subsaturated regions, and feeds back on the buoyancy through both latent heating and condensate loading.

Present study

The present study aims to fill this gap, bridging the classical Rayleigh–Bénard convection literature and the atmospheric convection literature through a simplified numerical framework that captures the essential mechanisms of moist convection while retaining a transparent connection to well-established laboratory-scale theory. The model, described in Chapter 2, is built on a Boussinesq one-fluid formulation derived from a two-phase flow solver, in which the liquid phase is retained as a prognostic volume-fraction field. Phase change is represented by a bulk relaxation of the vapour mass fraction toward its local saturation value, with the saturation state evaluated from the Antoine equation, so that condensation and evaporation occur over a finite relaxation time rather than instantaneously. The condensate is transported by the flow, settles with a prescribed terminal velocity following the treatment of Hernandez-Duenas et al. [48], and can re-evaporate where the gas is subsaturated. The buoyancy force includes the three moist contributions — thermal expansion, water-vapour content, and condensate loading — in a linearized form consistent with the formulation of Thomas et al. [50].

The total heat flux in the system is decomposed into two contributions: the sensible heat flux, which is what is typically measured in classical Rayleigh–Bénard experiments, and the latent heat flux, which reflects the thermodynamic contribution of phase-change processes [92]. Both contributions are studied simultaneously in the present work, allowing a more complete characterization of heat transport in moist convective systems than dry Rayleigh–Bénard studies alone can provide. For the cloud microphysics, a deliberately simplified representation is adopted: ice formation is neglected, droplet-scale processes such as size distributions and collision–coalescence are not resolved, and the liquid phase is described by a single bulk field. The fluid is assumed to have uniform effective diffusivities and viscosity throughout the domain. Dry convection is retained as a reference case throughout, allowing the isolated effect of moisture and phase change to be systematically assessed against a controlled baseline.

The novelty of this work therefore lies in retaining cloud liquid water as a prognostic field within a controlled Rayleigh–Bénard configuration: rather than removing condensate instantaneously, as in the Rainy–Bénard model of Vallis et al. [31], or transferring it immediately to rain, as in the fast-autoconversion models of Hernandez-Duenas et al. [48], the present framework resolves the finite lifetime of condensate in the flow. This allows the coupling between phase change, condensate loading, settling, re-evaporation, and buoyancy to be examined directly, while the underlying Rayleigh–Bénard configuration preserves the reproducibility and parameter-governed structure that make laboratory-scale convection theory tractable. In this way, the model offers a physically transparent yet complete bridge between idealized dry convection and the moist processes at the heart of atmospheric convective systems.

Chapter 2

Mathematical Formulation

2.1 Multiphase Flow Formulation

Multiphase flows involving heat and mass transfer arise in a wide range of natural and industrial processes, including atmospheric cloud formation, ocean evaporation, and turbulent precipitation [93, 94, 95, 96]. The accurate numerical representation of such flows requires a thermodynamically consistent framework capable of coupling fluid dynamics with phase-change processes. A well-established approach for achieving this is the use of conserved variables — quantities such as total mass, momentum, and energy — whose conservation properties are preserved exactly at the discrete level regardless of the phase state of the fluid. The general advantage of such conservative frameworks lies in their ability to ensure physically consistent coupling between compressible dynamics and phase-change processes, avoiding spurious sources or sinks of energy that can arise in non-conservative formulations. This philosophy is central to multiphase modelling strategies such as the Baer–Nunziato model [97], which employs separate conservation equations for the mass, momentum, and energy of each phase, and has been widely adopted in the modelling of compressible two-phase flows.

Multiphase flow methods can first be divided into resolved-interface approaches and unresolved-interface (mixture) approaches. In mixture models, the phases are represented by a volume fraction defined in each cell, whereas in resolved-interface methods the boundary between two fluids is explicitly represented and sharply identified. Resolved-interface methods are commonly categorized into interface tracking methods, such as Front Tracking, which follow the interface explicitly using Lagrangian markers, and interface capturing methods, such as the Volume-of-Fluid (VOF), Level-Set (LS), and Phase-Field (PF) approaches, in which the interface is represented implicitly through a transported scalar field. The VOF and LS approaches are generally regarded as sharp-interface methods, whereas Phase-Field methods belong to the diffuse-interface family. The present work instead uses a mixture (volume-fraction) formulation: within each computational cell the gas and liquid phases coexist, their relative amounts given by the volume fraction α_1, and no phase interface—sharp or diffuse—is resolved. This is the natural description for a cloudy flow, in which liquid water is present as a dilute condensate dispersed throughout the gas rather than as a separate region bounded by an interface. The formulation is detailed in Section 2.2.

The model considered in this project belongs to the class of Baer–Nunziato-type multiphase compressible flow models [97]. The fully compressible seven-equation two-phase flow model originally proposed by Baer and Nunziato, together with the formulation later developed by Saurel and Abgrall [98], represents one of the most general Eulerian frameworks for compressible multiphase flows. In this approach, the phases are treated as interpenetrating continua and are described through separate conservation equations for mass, momentum, and energy, resulting in a system of seven equations [99]. Unlike sharp-interface approaches, the BN formulation belongs to the diffuse-interface family, where the interface is represented as a finite-thickness transition region with smoothly varying thermodynamic properties. Furthermore, the model allows for thermodynamic and mechanical non-equilibrium between phases, accounting for differences in velocity, pressure, temperature, and chemical potential. Owing to these characteristics, BN-type models are particularly suitable for compressible and low-Mach multiphase flows involving evaporation, boiling, cavitation, and large density ratios.

Table 2.1: Comparison of 4-, 5-, 6-, and 7-equation multiphase flow models.

Model	No. Mass Eq.	No. Momentum Eq.	No. Energy Eq.	No. Volume Frac. Eq.
4-equation	2	1	1	0
5-equation	2	1	1	1
6-equation	2	1	2	1
7-equation	2	2	2	1

Diffuse-interface models for compressible two-phase flows exist at different levels of complexity depending on the equilibrium assumptions imposed between the phases. The most general formulation is the seven-equation Baer–Nunziato (BN) model [97], which allows full thermodynamic and mechanical non-equilibrium between phases. In this framework, each phase possesses its own conservation equations for mass, momentum, and energy, together with a volume-fraction transport equation. Interfacial exchange processes, such as momentum, pressure, heat, and mass transfer, are represented through relaxation source terms driving the system toward equilibrium.

By assuming instantaneous equilibrium for selected variables, simplified models can be derived from the BN system. The six-equation model assumes kinematic equilibrium between phases, while the five-equation model further assumes mechanical equilibrium. A further simplification leads to the four-equation model, which assumes kinematic , mechanical, and thermal equilibrium while still retaining chemical non-equilibrium, allowing the description of phase change and mass transfer processes. These reduced models provide lower computational cost while preserving the essential physics required for many compressible multiphase flow applications.

2.2 Parent Four-Equation Multiphase Model

The atmospheric model developed in this work is not constructed from first principles in isolation, but is obtained as a reduction of a more general multiphase framework. This section introduces that parent model and the equilibrium assumptions that connect it to the atmospheric formulation of Section 2.3. Establishing this lineage clarifies where the governing equations originate, why the flow is described in terms of phase volume fractions, and which physical effects are retained or discarded in the present study.

The parent model is the four-equation diffuse-interface model for compressible two-phase flows introduced in Section 2.1. In compressible flows, the fluid density varies in space and time due to changes in pressure, temperature, or composition, so that pressure, temperature, and density are coupled and the velocity field is not, in general, divergence-free, $\nabla \cdot \boldsymbol{u} \neq 0$. The importance of compressibility is characterized by the Mach number, $Ma = U/c$, where U is a characteristic flow velocity and c is the speed of sound. As noted above, the four-equation model is obtained from the seven-equation Baer–Nunziato model by assuming instantaneous velocity, pressure, and temperature relaxation between the phases. As a result, the two phases are in kinematic , mechanical, and thermal equilibrium, while chemical non-equilibrium is retained so that mass transfer between phases, and hence phase change, can still be described.

Let α_k, ρ_k, and $\mathcal{E}_k$ denote the volume fraction, density, and internal energy per unit volume of phase k, with $k = 1, 2$. The common pressure, temperature, and velocity fields are denoted by p, T, and $\boldsymbol{u}$, respectively. The mixture density, internal energy, and total energy are

$$\rho = \sum_{k=1}^{2} \alpha_k \rho_k, \qquad \mathcal{E} = \sum_{k=1}^{2} \alpha_k \mathcal{E}_k, \qquad E = \sum_{k=1}^{2} \alpha_k E_k, \qquad E_k = \mathcal{E}_k + \tfrac{1}{2}\rho_k |\boldsymbol{u}|^2.$$

The conservative form of the model consists of two mass equations, a mixture momentum equation, and a mixture energy equation:

$$\partial_t(\alpha_1\rho_1) + \nabla \cdot (\alpha_1\rho_1\boldsymbol{u}) = \mathcal{M}, \tag{2.1a}$$

$$\partial_t(\alpha_2\rho_2) + \nabla \cdot (\alpha_2\rho_2\boldsymbol{u}) = -\mathcal{M}, \tag{2.1b}$$

$$\partial_t(\rho\boldsymbol{u}) + \nabla \cdot (\rho\boldsymbol{u} \otimes \boldsymbol{u} + p\boldsymbol{I}) = \nabla \cdot \boldsymbol{\tau} + \boldsymbol{\Sigma} + \rho\boldsymbol{g}, \tag{2.1c}$$

$$\partial_t E + \nabla \cdot [(E + p)\boldsymbol{u}] = \nabla \cdot (\boldsymbol{\tau} \cdot \boldsymbol{u}) - \nabla \cdot \boldsymbol{q} + \boldsymbol{\Sigma} \cdot \boldsymbol{u} + \rho\boldsymbol{g} \cdot \boldsymbol{u}. \tag{2.1d}$$

Here $\mathcal{M}$ is the interfacial mass-transfer term, with a positive value corresponding to mass transfer from phase 2 to phase 1. The mixture viscous stress tensor is $\boldsymbol{\tau} = \alpha_1\boldsymbol{\tau}_1 + \alpha_2\boldsymbol{\tau}_2$ and, assuming a Newtonian constitutive law,

$$\boldsymbol{\tau} = \mu\left[\nabla\boldsymbol{u} + (\nabla\boldsymbol{u})^T\right] - \frac{2}{3}\mu(\nabla \cdot \boldsymbol{u})\boldsymbol{I}, \qquad \mu = \alpha_1\mu_1 + \alpha_2\mu_2.$$

The surface-tension force is modelled as $\boldsymbol{\Sigma} = \sigma\kappa\nabla\alpha_1$, where σ is the surface-tension coefficient and $\kappa = -\nabla\cdot(\nabla\alpha_1/|\nabla\alpha_1|)$ is the local interface curvature. Heat conduction follows Fourier's law, $\boldsymbol{q} = -\lambda_c\nabla T$, with the mixture thermal conductivity $\lambda_c = \alpha_1\lambda_{c1} + \alpha_2\lambda_{c2}$.

The model is closed by assigning an equation of state to each phase, $p_k = p_k(\mathcal{E}_k, \rho_k)$ and $T_k = T_k(\mathcal{E}_k, \rho_k)$. Because the phases are assumed to be in mechanical and thermal equilibrium, the phase pressures and temperatures satisfy

$$p_1 = p_2 = p, \qquad T_1 = T_2 = T.$$

Closing the fully compressible system additionally requires a mixture speed of sound and an equivalent pressure- (or enthalpy-) evolution equation, together with the associated thermodynamic coefficients; these are not required for the incompressible reduction used here, and the reader is referred to Salimi et al. [100] for the complete compressible closure.

This parent formulation belongs to the class of interface-unresolved, or mixture, models: the sharp boundary between phases is not explicitly tracked, but is instead represented by the volume fraction of each phase, which varies smoothly over several computational cells. Rather than following a sharp interface, the method tracks the transition from one fluid to another and describes the averaged behaviour of the phases, with each phase carrying its own contribution to mass, momentum, and energy.

From this parent model, the atmospheric formulation of Section 2.3 is obtained through a sequence of simplifications appropriate to shallow, low-speed moist convection. The equilibrium assumptions have already been imposed in deriving the four-equation system (2.1), so that a single velocity, pressure, and temperature describe the flow. The remaining simplifications are as follows: the low-Mach-number limit is taken, filtering acoustic modes; surface tension and gas-phase compressibility are neglected, the latter leading to a divergence-free velocity field while retaining density variations in the buoyancy term through the Boussinesq approximation; and the regularization terms of the diffuse-interface treatment are dropped. Chemical non-equilibrium is retained throughout, so that condensation and evaporation are still represented through the mass-transfer term $\mathcal{M}$. The resulting one-fluid Boussinesq equations, together with the buoyancy and phase-change closures specific to moist convection, are presented in the following section. These simplifications remove acoustic dynamics and interface-scale effects while retaining the essential coupling between buoyancy, moisture transport, latent heating, and phase change that governs moist atmospheric convection.

2.3 Two-phase Atmospheric Flows

In this work, we employ the model developed by Salimi et al. [100], who formulated a low-Mach-number, four-equation solver to simulate multiphase, multicomponent flows with phase change. The interface is captured using an implicit diffuse-interface approach based on the volume-fraction formulation, supplemented by regularization terms. This framework allows for the simulation of two-phase flows involving a liquid–gas interface undergoing phase change. In particular, it accounts for gas-phase compressibility effects within the low-Mach-number approximation, while the liquid phase is treated as incompressible.

In the present study, the gas-phase compressibility effects and regularization terms of the previous model are neglected. The system is described within a one-fluid formulation, whereby a single velocity field $\boldsymbol{u}$, temperature T, and pressure p represent the entire flow. This implies local mechanical and thermal equilibrium between the phases, and kinematic equilibrium apart from a prescribed droplet settling velocity, while chemical non-equilibrium is retained to account for phase change. Under these assumptions, the governing equations can be written in conservative form as follows:

$$\frac{\partial \alpha_1}{\partial t} + \boldsymbol{\nabla} \cdot \left[\alpha_1 \left(\boldsymbol{u} - w_T \hat{\boldsymbol{z}}\right)\right] = \frac{\mathcal{M}}{\rho_1}, \tag{2.2}$$

$$\frac{\partial(\alpha_2 \rho_2 \xi)}{\partial t} + \boldsymbol{\nabla} \cdot \left(\alpha_2 \rho_2 \xi \, \boldsymbol{u}\right) = -\mathcal{M} + \boldsymbol{\nabla} \cdot \left(\alpha_2 \rho_2 D_{va} \boldsymbol{\nabla} \xi\right), \tag{2.3}$$

$$\frac{\partial(\rho_2 \boldsymbol{u})}{\partial t} + \boldsymbol{\nabla} \cdot \left(\rho_2 \, \boldsymbol{u} \otimes \boldsymbol{u}\right) = -\boldsymbol{\nabla} p + \boldsymbol{\nabla} \cdot \boldsymbol{\tau} + \rho_b \, \boldsymbol{g}, \tag{2.4}$$

$$\boldsymbol{\nabla} \cdot \boldsymbol{u} = 0, \tag{2.5}$$

$$\frac{\partial(\rho c_p T)}{\partial t} + \boldsymbol{\nabla} \cdot \left(\rho c_p \, \boldsymbol{u} T\right) = \boldsymbol{\nabla} \cdot \left(\lambda_c \boldsymbol{\nabla} T\right) + \mathcal{M} L. \tag{2.6}$$

Here, subscripts 1 and 2 denote the liquid and gaseous phases, respectively. The corresponding volume fractions satisfy

$$\alpha_1 + \alpha_2 = 1. \tag{2.7}$$

The liquid density ρ_1 and gas density ρ_2 are both assumed constant. The gas phase is treated as a mixture of water vapour and a non-condensable gas (dry air). Consistent with the Boussinesq approximation, a single constant reference gas density ρ_2 is used both in the inertial terms of the momentum equation (2.4) and in the vapour-transport equation (2.3). This reference density is evaluated as the pure dry-air density at the reference temperature T_0, and because the reference vapour content is small it is well approximated by this value, $\rho_2 \approx \rho_{\mathrm{air}}(T_0)$, so that the gas-density variations associated with vapour content are retained only in the buoyancy term through the coefficient ϵ_ξ introduced in Section 2.3.1. The effective density ρ_b is the variable density retained in the gravitational body force, and is likewise discussed further in Section 2.3.1.

The first equation includes the sedimentation of liquid water through the terminal velocity w_T, following the form used in cloudy Rayleigh–Bénard and precipitating-convection models by Thomas et al. [50] and Hernandez-Duenas et al. [48]. Here, $w_T > 0$ denotes the magnitude of the downward terminal speed of liquid droplets. Since $\hat{\boldsymbol{z}}$ is defined to point upward, the settling velocity of the liquid phase is $-w_T\hat{\boldsymbol{z}}$. When the liquid-water volume fraction exceeds a prescribed critical value, the liquid phase is transported with the velocity

$$\boldsymbol{u}_\ell = \boldsymbol{u} - w_T\hat{\boldsymbol{z}}. \tag{2.8}$$

In principle, the terminal velocity can be related to the droplet radius using the Stokes settling velocity,

$$w_T = \frac{2(\rho_1 - \rho_2)gR^2}{9\mu_2}, \tag{2.9}$$

where R is the droplet radius and μ_2 is the dynamic viscosity of the gas phase. If the droplet number concentration N is assumed constant, the liquid volume fraction satisfies

$$\alpha_1 = N\frac{4}{3}\pi R^3, \tag{2.10}$$

and therefore

$$w_T = \frac{2(\rho_1 - \rho_2)g}{9\mu_2}\left(\frac{3\alpha_1}{4\pi N}\right)^{2/3}. \tag{2.11}$$

Thus, under the assumption of constant N, the terminal velocity scales as $w_T \propto \alpha_1^{2/3}$.

However, in the present work, for simplicity and following the approach of Hernandez-Duenas et al. [48], the terminal velocity is prescribed as a constant parameter rather than being computed from the local liquid volume fraction or droplet-size distribution. A comparable treatment is adopted by Thomas et al. [50], who prescribe the terminal velocity as a constant non-dimensional settling number (a dimensionless Rouse-type parameter), varied over the range 0.01 to 0.9 to span conditions from slowly settling, cloud-like droplets to rapidly falling, rain-like drops.

The vapour mass fraction ξ is treated as a transported scalar defined over the entire domain as

$$\xi = \frac{m_v}{m_2}, \tag{2.12}$$

where m_v is the mass of water vapour and m_2 is the mass of the gas phase. The parameter D_{va} denotes the mass diffusion coefficient of water vapour in air. The tensor $\boldsymbol{\tau}$ denotes the viscous stress tensor, and $\boldsymbol{g}$ represents the gravitational acceleration.

The mass transfer is represented by the source term $\mathcal{M}$, which accounts for phase change (further details are provided in Section 2.3.2). The latent heat of vaporization is denoted by L. The mixture properties in the energy equation are defined as

$$\lambda_c = \alpha_1 \lambda_1 + \alpha_2 \lambda_2, \tag{2.13}$$

$$\rho c_p = \alpha_1 \rho_1 c_{p,1} + \alpha_2 \rho_2 c_{p,2}, \tag{2.14}$$

where λ_c is the effective thermal conductivity and c_p is the specific heat capacity of the mixture.

2.3.1 Boussinesq approximation

In the present model, the two-phase system is described by a single temperature field, consistent with the assumption of local thermal equilibrium between phases. Density variations are assumed to be small compared with the reference density and are therefore neglected in the inertial and continuity equations, consistent with the Boussinesq approximation. In atmospheric cloud-resolving models, especially when the vertical extent is large enough for the background density to vary appreciably with height, the anelastic approximation is often adopted instead; in that case, a height-dependent reference density is retained, as in the model used by Thomas et al. [50]. In the present configuration, however, the domain height is small compared with the density scale height and the imposed temperature difference is moderate, such that $\beta_{\mathrm{th}} \Delta T \ll 1$. The background density can therefore be treated as essentially uniform, and the Boussinesq approximation is adequate, as also adopted in related idealized moist-convection studies by Vallis et al. [31] and Hernandez-Duenas et al. [48].

Within the Boussinesq approximation, the density is treated as constant in the inertial and advective terms, while its variations are retained only in the gravitational body force. In moist convection, the density variation is associated with three contributions: thermal expansion, water-vapour content, and condensate loading. This decomposition is consistent with the buoyancy formulation used in the idealized cloudy Rayleigh–Bénard model of Thomas et al. [50], in which temperature, vapour, and liquid-water terms contribute separately to the buoyancy force [31, 48].

Considering the momentum equation (2.4), the buoyancy density can be written in linearized form about the reference state (T_0, ξ_0) as

$$\rho_b = \alpha_1 \rho_1 + (1 - \alpha_1) \rho_2 \left[1 - \beta_{\mathrm{th}}(T - T_0) - \epsilon_\xi (\xi - \xi_0)\right]. \tag{2.15}$$

Here, ρ_2 denotes the reference gas density, which is constant and evaluated at the reference vapour mass fraction ξ_0,

$$\rho_2 \equiv \rho_g(\xi_0), \tag{2.16}$$

where

$$\rho_g(\xi) = \left[\frac{\xi}{\rho_{\mathrm{vap}}} + \frac{1 - \xi}{\rho_{\mathrm{air}}}\right]^{-1}. \tag{2.17}$$

Here, ρ_{vap} and ρ_{air} denote the reference densities of pure water vapour and dry air, respectively, and are treated as constants.

The term $\alpha_1\rho_1$ represents the condensate-loading contribution. Since the liquid phase is incompressible, it contributes through its weight per unit volume. The coefficient ϵ_ξ measures the sensitivity of the gas density to changes in vapour mass fraction. For an ideal-gas mixture close to dry air, this coefficient is approximately

$$\epsilon_\xi \simeq \frac{R_v}{R_d} - 1 = \frac{M_d}{M_v} - 1 \simeq 0.61, \tag{2.18}$$

where R_v and R_d are the specific gas constants of water vapour and dry air, and M_v and M_d are their molar masses. The isobaric thermal expansion coefficient of the gas phase is taken as constant, $\beta_{\text{th}} = 1/T_0$, consistent with the ideal-gas value at the reference temperature and with the small density variations assumed in the Boussinesq limit. The term proportional to $\beta_{\text{th}}(T - T_0)$ represents the thermal contribution, which reduces the gas density when the temperature is higher than the reference value T_0. The term proportional to $\epsilon_\xi(\xi - \xi_0)$ represents the water-vapour contribution, which reduces the gas density when the vapour content is higher than the reference value ξ_0.

Alternatively, the water-vapour contribution can be retained without linearizing the gas density with respect to ξ. In this case, the dependence of the gas-phase density on vapour content is evaluated using Amagat's law of additive volumes. The buoyancy density is then written as

$$\rho_b = \alpha_1\rho_1 + (1 - \alpha_1)\rho_g(\xi)\left[1 - \beta_{\text{th}}(T - T_0)\right]. \tag{2.19}$$

Since ξ is the vapour mass fraction, Eq. (2.17) represents a mass-fraction-weighted specific-volume relation. Because water vapour is lighter than dry air, $\rho_{\text{vap}} < \rho_{\text{air}}$, an increase in ξ decreases $\rho_g(\xi)$ and therefore reduces the effective gas density, corresponding to the usual virtual-temperature effect. In this exact-composition form, the vapour effect is included directly through $\rho_g(\xi)$ rather than through the linearized coefficient ϵ_ξ. To connect this expression to the implemented linearized form, $\rho_g(\xi)$ is expanded about the reference vapour mass fraction ξ_0 using a first-order Taylor approximation:

$$\left.\frac{d\rho_g}{d\xi}\right|_{\xi_0} = -\rho_g^2(\xi_0)\left(\frac{1}{\rho_{\text{vap}}} - \frac{1}{\rho_{\text{air}}}\right). \tag{2.20}$$

Substituting this result into the expansion, and using $\rho_2 \equiv \rho_g(\xi_0)$, gives

$$\rho_g(\xi) \approx \rho_2\left[1 - \epsilon_\xi(\xi - \xi_0)\right], \tag{2.21}$$

where

$$\epsilon_\xi = \rho_2\left(\frac{1}{\rho_{\text{vap}}} - \frac{1}{\rho_{\text{air}}}\right). \tag{2.22}$$

Because water vapour is lighter than dry air, $\rho_{\text{vap}} < \rho_{\text{air}}$, the coefficient ϵ_ξ is positive; thus, an increase in ξ reduces the gas density. Including the linearized thermal dependence gives

$$\rho_g(T,\xi) \approx \rho_2 \left[1 - \epsilon_\xi(\xi - \xi_0)\right]\left[1 - \beta_{\mathrm{th}}(T - T_0)\right]. \tag{2.23}$$

Expanding this product gives

$$\rho_g(T,\xi) \approx \rho_2 \left[1 - \beta_{\mathrm{th}}(T - T_0) - \epsilon_\xi(\xi - \xi_0) + \beta_{\mathrm{th}}\epsilon_\xi(T - T_0)(\xi - \xi_0)\right]. \tag{2.24}$$

The last term is a product of two small perturbations and is therefore a second-order contribution. Neglecting this term gives the first-order linearized gas-density relation

$$\rho_g(T,\xi) \approx \rho_2 \left[1 - \beta_{\mathrm{th}}(T - T_0) - \epsilon_\xi(\xi - \xi_0)\right]. \tag{2.25}$$

Substituting Eq. (2.25) into the phase-volume-weighted density gives the buoyancy density used in the present implementation:

$$\rho_b = \alpha_1\rho_1 + (1 - \alpha_1)\rho_2 \left[1 - \beta_{\mathrm{th}}(T - T_0) - \epsilon_\xi(\xi - \xi_0)\right]. \tag{2.26}$$

Therefore, with $\rho_2 \equiv \rho_g(\xi_0)$, and neglecting second-order products such as $(T - T_0)(\xi - \xi_0)$, the linearized expression in Eq. (2.15) is recovered as the first-order Taylor approximation of Eq. (2.19) about ξ_0.

In the present implementation, the linearized form in Eq. (2.15) is adopted. The exact Amagat form in Eq. (2.19) is introduced only to motivate the definition of the vapour-sensitivity coefficient ϵ_ξ and to show its connection with the underlying gas-mixture density. Thus, the vapour effect is not counted twice: either it is represented directly through $\rho_g(\xi)$ in the exact-composition form, or through the linearized term $\epsilon_\xi(\xi - \xi_0)$ in the implemented form.

2.3.2 Phase change relations

The mass transfer term $\mathcal{M}$ can be modelled in different ways. Following Salimi et al. [100], it can be expressed based on the relaxation of the chemical potentials between the liquid (denoted by l) and vapour (denoted by v) phases:

$$\mathcal{M} = \frac{1}{\Omega_\mu \tau_\mu}\left(\mu_v^p - \mu_l^p\right), \tag{2.27}$$

where μ_v^p and μ_l^p are the chemical potentials of the vapour and liquid phases, respectively, and τ_μ and Ω_μ are relaxation parameters.

The chemical potential difference can be related to thermodynamic variables as

$$\Delta\mu^p = \frac{R}{M_v} T \log\left(\frac{pX_v}{p_{\mathrm{sat}}(T)}\right), \tag{2.28}$$

where R is the universal gas constant, M_v is the molar mass of vapour, and X_v is the vapour molar fraction. Imposing thermodynamic equilibrium, $\Delta\mu^p = 0$, yields

$$X_{v,\mathrm{sat}} = \frac{p_{\mathrm{sat}}(T)}{p}. \tag{2.29}$$

Assuming that the liquid specific volume is negligible compared to that of the vapour, the above relation remains valid and allows the equilibrium vapour molar fraction to be expressed solely as a function of pressure and temperature.

Based on this, an alternative formulation of the mass transfer term can be written in terms of the vapour mass fraction ξ [31]:

$$\mathcal{M} = \frac{1}{\tau_\xi}\left(\xi - \xi_{\mathrm{sat}}\right), \tag{2.30}$$

where the relaxation rate $1/\tau_\xi$ drives the system toward thermodynamic equilibrium defined by the saturation mass fraction ξ_{sat}. The sign of $\mathcal{M}$ determines the direction of phase change. When the gas phase is supersaturated, $\xi > \xi_{\mathrm{sat}}$, the mass-transfer term is positive, $\mathcal{M} > 0$, and water vapour is converted into liquid water, corresponding to condensation. Conversely, when the gas phase is subsaturated, $\xi < \xi_{\mathrm{sat}}$, the mass-transfer term is negative, $\mathcal{M} < 0$, and liquid water evaporates into the gas phase. At saturation, $\xi = \xi_{\mathrm{sat}}$, the system is in local thermodynamic equilibrium and $\mathcal{M} = 0$.

The saturation vapour mass fraction is related to the molar fraction as

$$\xi_{\mathrm{sat}} = \frac{X_{v,\mathrm{sat}}}{X_{v,\mathrm{sat}} + (1 - X_{v,\mathrm{sat}})\frac{M_a}{M_v}} = \frac{p_{\mathrm{sat}}(T)}{p_{\mathrm{sat}}(T) + (p_0(z) - p_{\mathrm{sat}}(T))\frac{M_a}{M_v}}, \tag{2.31}$$

where M_a is the molar mass of the non-condensable gas (air), and the total pressure has been approximated by the background hydrostatic pressure $p_0(z)$. The background pressure $p_0(z)$ is assumed to satisfy hydrostatic balance [27],

$$\frac{dp_0(z)}{dz} = -\rho_0(z)\, g, \tag{2.32}$$

where $\rho_0(z)$ is the reference density. The saturation pressure $p_{\mathrm{sat}}(T)$ is evaluated using the Antoine equation:

$$\log_{10} p_{\mathrm{sat}} = A_A - \frac{B_A}{C_A + T}, \tag{2.33}$$

where A_A, B_A, and C_A are empirical coefficients and T is the local temperature. In the present study, this formulation is adopted to close the governing equations.

Chapter 3

Results

3.1 Simulation parameters

The objective of this study is to contrast two convective regimes: a *dry* case, in which no phase change takes place and the flow is driven by thermal buoyancy alone, and a *moist* case, in which condensation and evaporation are active together with the associated latent heating and condensate loading. The distinction between the two regimes lies in the presence of phase change rather than in the presence of water vapour itself: water vapour is carried in both cases, but in the dry case it is not permitted to condense, so that no latent heat is released and no liquid water forms. The configuration is intended as an idealised model of *shallow* atmospheric convection—the regime of fair-weather cumulus and the cloud-topped boundary layer, in which moist overturning is confined to a layer of the order of a few hundred metres to a kilometre deep, well below the scale of deep convective towers. This regime is particularly suited to a controlled study because the relevant dynamics can be captured in a compact domain while still retaining the essential moist physics: the lifting of near-surface air to saturation, condensation and the associated latent heating, and the buoyancy modification produced by both water vapour and suspended cloud water. Restricting attention to shallow convection also keeps the vertical extent small enough that the Boussinesq approximation remains an appropriate framework, since density variations across the layer stay modest.

Both simulations are performed in the same quasi-two-dimensional vertical convection domain, with height $H = 500$ m and horizontal extent 500 m. The lower and upper walls are maintained at 295 K and 285 K, respectively, corresponding to an imposed temperature difference of $\Delta T = 10$ K. The two cases differ only in their moisture treatment. The dry run is a non-condensing thermal reference, whereas the moist run includes saturated vapour boundary conditions and active phase change. This setup makes it possible to isolate the additional effects of moist physics—latent-heat release during condensation and condensate loading in the buoyancy force—from the purely thermal Rayleigh–Bénard dynamics.

The simulations are performed in two dimensions, in the vertical (x, z) plane aligned with gravity. The square domain gives an aspect ratio of unity, $\Gamma = L_x/L_z =$

1, which admits a small number of large-scale convective cells while keeping the computation tractable and the comparison between the two cases clean. Although a genuinely three-dimensional calculation would be required to capture the full turbulent cascade, the two-dimensional setting retains the essential large-scale buoyancy-driven overturning and the moist thermodynamic feedbacks that are the focus of this work, and it is a standard idealisation for Rayleigh–Bénard and moist-convection studies. The lateral boundaries are periodic, so that the flow is statistically homogeneous in the horizontal and free of artificial sidewall effects. At the top and bottom walls a no-slip, impermeable condition is imposed on the velocity field, and the temperature is held fixed at the prescribed wall values, providing the Dirichlet thermal forcing that drives the convection.

The two cases differ in the boundary condition imposed on the vapour field. In the dry reference case, phase change is disabled and a zero-flux (Neumann) condition, $\partial_z \xi = 0$, is applied to the vapour at both walls, so that no net moisture is exchanged with the boundaries and the total vapour content is conserved. In the moist case, a Dirichlet condition is imposed on the vapour at both walls, with the vapour mass fraction held at its local saturation value, $\xi = \xi_{\mathrm{sat}}(T_{\mathrm{wall}})$, corresponding to a relative humidity of 100% at both the lower and upper plates. Because the two walls are held at different temperatures, and hence at different saturation values, this fully saturated condition still establishes a vertical vapour gradient between the plates that drives moisture transport through the interior.

Rather than resolving the full molecular dissipation range, the present calculations are carried out as a coarse-grained, pseudo-DNS model in which the small-scale turbulent transport is represented through effective eddy coefficients. This choice is physically motivated. In the atmosphere the Reynolds number is extremely large, and the molecular values of viscosity and of the thermal and vapour diffusivities are many orders of magnitude smaller than their turbulent counterparts. Outside the thin near-surface layers where molecular processes act, the transport of momentum, heat, and moisture across the bulk of the convective layer is overwhelmingly accomplished by turbulent eddies, and the molecular diffusivities play essentially no role in setting the large-scale structure of the flow. It is therefore both consistent and computationally advantageous to replace them with effective eddy coefficients that represent the aggregate action of the unresolved subgrid motions. Only the large-scale convective overturning is resolved explicitly, while the smaller scales are parameterised through an eddy viscosity ν_t, an eddy thermal diffusivity κ_t, and an eddy mass (vapour) diffusivity D_t. A direct consequence is that the Rayleigh number reported here is an *effective* turbulent Rayleigh number, built on the eddy diffusivities rather than the molecular ones; the molecular Rayleigh number for a layer of this depth and temperature contrast would be prohibitively large and is not the quantity that governs the resolved dynamics. The physical realism of the model thus resides in the thermodynamic closure—a realistic temperature contrast, domain scale, and saturation relation—rather than in the resolution of the molecular dissipation range.

The three eddy coefficients are not specified independently. Once the eddy viscosity is chosen, the thermal and mass diffusivities follow from the turbulent Prandtl and Schmidt numbers,

$$\kappa_t = \frac{\nu_t}{\mathrm{Pr}_t}, \qquad D_t = \frac{\nu_t}{\mathrm{Sc}_t}, \tag{3.1}$$

so that prescribing Pr_t and Sc_t fixes the relative efficiency of momentum, heat, and vapour transport. We adopt $\mathrm{Pr}_t \approx 0.7$ and $\mathrm{Sc}_t \approx 0.6$, values that lie within the ranges reported for the atmospheric boundary layer [50, 101, 102, 103]. Because the same Pr_t and Sc_t, and hence the same eddy coefficients, are imposed in both runs, the turbulent mixing is identical across the two cases.

The two cases are characterised by a set of dimensionless control parameters, summarised together with the physical inputs in Table 3.1 and listed for each run in Table 3.2. The effective Rayleigh number,

$$Ra = \frac{g\,\beta_t\,\Delta T\,H^3}{\nu_t\,\kappa_t}, \tag{3.2}$$

measures the strength of buoyant forcing relative to diffusive damping; with the eddy coefficients adopted here it takes the value $Ra \approx 3 \times 10^7$, placing the flow well into the turbulent regime. The turbulent Prandtl and Schmidt numbers, $\mathrm{Pr}_t = \nu_t/\kappa_t$ and $\mathrm{Sc}_t = \nu_t/D_t$, set the relative efficiency of heat and vapour mixing.

The adequacy of the spatial resolution is assessed against the Kolmogorov length scale, estimated from the global dissipation balance for Rayleigh–Bénard convection. In a statistically steady state the mean kinetic-energy dissipation rate is fixed by the heat transport, $\varepsilon = (\nu_t^3/H^4)(Nu-1)\,Ra\,\mathrm{Pr}_t^{-2}$, so that the Kolmogorov scale can be written as [73, 104]

$$\eta = \left(\frac{\nu_t^3}{\varepsilon}\right)^{1/4} = H\,\mathrm{Pr}_t^{1/2}\,(Nu-1)^{-1/4}\,Ra^{-1/4}. \tag{3.3}$$

With $Ra \approx 3 \times 10^7$, $\mathrm{Pr}_t = 0.7$, and the measured $Nu \approx 13$, this yields $\eta \approx 3$ m. The grid spacing adopted here, $\Delta = H/N_z \approx 2$ m (isotropic in all three directions), therefore satisfies $\Delta \lesssim \eta$, so that the effective dissipation scale is resolved on the computational grid [104]. Since the unresolved small-scale transport is in any case represented through the eddy coefficients rather than resolved down to the molecular dissipation range, this resolution is more than adequate to capture the energy-containing convective motions that govern the resolved dynamics, consistent with the coarse-grained, pseudo-DNS character of the model.

For the moist case, two further parameters describe the phase-change physics. The Damköhler number, $Da = t_0/\tau$, compares the convective time scale $t_0 = H/U_0$ to the phase-change relaxation time τ; a value $Da = 1$ would indicate that condensation and evaporation relax towards equilibrium on the convective turnover time. The Stefan number St measures the latent heat released by condensation relative to the sensible-heat scale $c_p\Delta T$ [50]. In the dry case no phase change occurs, so Da and St are inactive.

Table 3.1: Physical parameters for the $H = 500$ m setup at $\Delta T = 10$ K.

Parameter	**Value**	**Units**
Flow and scaling parameters		
Reference length H	500	m
Temperature scale ΔT	10	K
Reference velocity $U_0 = (g\beta_t \Delta T H)^{1/2}$	13	$\mathrm{m\,s^{-1}}$
Time scale $t_0 = H/U_0$	38	s
Eddy viscosity ν_t	1	$\mathrm{m^2\,s^{-1}}$
Eddy thermal diffusivity $\kappa_t = \nu_t/\mathrm{Pr}_t$	1.43	$\mathrm{m^2\,s^{-1}}$
Eddy mass diffusivity $D_t = \nu_t/\mathrm{Sc}_t$	1.67	$\mathrm{m^2\,s^{-1}}$
Thermodynamic constants		
Latent heat L_v	2.5×10^6	$\mathrm{J\,kg^{-1}}$
Thermal expansion (gas) $\beta_t \approx 1/T_0$	3.45×10^{-3}	$\mathrm{K^{-1}}$
Reference temperature T_0	290	K
Reference pressure p_0	10^5	Pa
Gravity g	9.8	$\mathrm{m\,s^{-2}}$
Sat. mass fraction $\xi_{\mathrm{sat}}(295\,\mathrm{K})$ (bottom)	1.65×10^{-2}	–
Sat. mass fraction $\xi_{\mathrm{sat}}(285\,\mathrm{K})$ (top)	8.7×10^{-3}	–
Gas phase properties		
Density ρ_g	1.18	$\mathrm{kg\,m^{-3}}$
Specific heat $c_{p,g}$	1004	$\mathrm{J\,kg^{-1}\,K^{-1}}$
Specific heat $c_{v,g}$	718	$\mathrm{J\,kg^{-1}\,K^{-1}}$
Thermal conductivity λ_g	0.026	$\mathrm{W\,m^{-1}\,K^{-1}}$
Kinematic viscosity ν_g	1.5×10^{-5}	$\mathrm{m^2\,s^{-1}}$
Thermal diffusivity κ_g	2.1×10^{-5}	$\mathrm{m^2\,s^{-1}}$
Liquid phase properties		
Density ρ_l	1000	$\mathrm{kg\,m^{-3}}$
Specific heat $c_{p,l}$	4180	$\mathrm{J\,kg^{-1}\,K^{-1}}$
Thermal conductivity λ_l	0.6	$\mathrm{W\,m^{-1}\,K^{-1}}$
Kinematic viscosity ν_l	1.0×10^{-6}	$\mathrm{m^2\,s^{-1}}$
Thermal diffusivity κ_l	1.4×10^{-7}	$\mathrm{m^2\,s^{-1}}$
Thermal expansion β_l	2.76×10^{-4}	$\mathrm{K^{-1}}$
Mass transfer		
Molecular vapour diffusivity D	2.8×10^{-5}	$\mathrm{m^2\,s^{-1}}$

The saturation vapour content at the two walls follows directly from the phase-change closure of Section 2.3.2. Each wall temperature is fixed—$T_{\text{bot}} = 295\,\text{K}$ at the lower plate and $T_{\text{top}} = 285\,\text{K}$ at the upper plate—and the saturation vapour pressure $p_{\text{sat}}(T)$ is evaluated from the Antoine equation, Eq. (2.33); the saturation vapour mass fraction ξ_{sat} then follows from Eq. (2.31) with the background pressure fixed at $p_0 = 10^5\,\text{Pa}$. This yields $p_{\text{sat}} \approx 2.6 \times 10^3\,\text{Pa}$ and $\xi_{\text{sat}} \approx 1.65 \times 10^{-2}$ at the lower wall, and $p_{\text{sat}} \approx 1.4 \times 10^3\,\text{Pa}$ and $\xi_{\text{sat}} \approx 8.7 \times 10^{-3}$ at the upper wall, so that the imposed temperature contrast also establishes a saturation gradient between the plates. The two runs are distinguished by their vapour boundary condition and initial humidity: the dry reference case is initialised at RH = 80% with phase change disabled and a zero-flux vapour condition at the walls, while the moist case holds both walls at saturation (RH = 100%) with condensation active, the initial vapour mass fraction being $\xi_0 = \text{RH}\,\xi_{\text{sat}}(T)$ evaluated at the local temperature.

Both simulations are carried out on the same computational grid of $N_x \times N_y \times N_z = 4 \times 256 \times 256$ cells over the $500 \times 500\,\text{m}$ domain, giving an isotropic mesh spacing of $\Delta = H/N_z \approx 2\,\text{m}$ in all three directions. As established in the discussion of Eq. (3.3), this spacing satisfies the Kolmogorov resolution criterion, $\Delta \lesssim \eta$, with the effective Kolmogorov scale $\eta \approx 3\,\text{m}$ at $Ra \approx 3 \times 10^7$; the effective dissipation scale is therefore resolved on the grid in both cases. The two cases are summarised in Table 3.2.

Table 3.2: The two two-dimensional cases: a dry reference and a moist run.

Case	Type	RH	Vapour BC	Ra	Pr	Sc	Da	St
D1	dry	80%	Neumann	3.0×10^7	0.7	0.6	–	–
M1	moist	100%	Dirichlet (sat.)	3.0×10^7	0.7	0.6	0.1	10^{-3}

The primary diagnostic used to quantify vertical transport is the Nusselt number, the standard dimensionless measure of convective efficiency. It expresses the total vertical energy flux carried across the layer as a multiple of the flux that pure conduction alone would carry under the same temperature contrast, so that $Nu = 1$ corresponds to a motionless, purely conductive state and $Nu > 1$ measures the enhancement of transport by convective motion [49]. In classical dry Rayleigh–Bénard convection it is defined as the ratio of the total sensible heat flux to the conductive reference flux across the same layer, and it therefore provides a compact, geometry-independent measure of how strongly buoyancy-driven overturning augments heat transport.

The Nusselt number is particularly well suited to comparing the dry and moist runs, because it reduces both to a single transport efficiency measured against a common baseline. The dry case transports energy by sensible heat alone, whereas the moist case transports both sensible heat and the latent energy carried by water vapour. To ensure that any difference between the two reflects the physics of phase change rather than a different choice of normalisation, all fluxes in both runs are referred to the same dry conductive reference flux,

$$q_{\text{ref}} = \lambda_{\text{ref}} \frac{\Delta T}{H}, \tag{3.4}$$

where $\lambda_{\text{ref}} = \rho_g c_{p,g} \kappa_t$ is the effective (eddy) thermal conductivity of the gas, $\Delta T =$ 10 K is the imposed temperature difference, and $H = 500$ m is the domain height. With the gas-phase properties of Table 3.1, the corresponding reference conductive heat flux is $q_{\text{ref}} \approx 34.4\ \text{W m}^{-2}$. Because q_{ref} is identical for the two simulations, the dry and moist Nusselt numbers are evaluated on exactly the same basis, so that any difference between them reflects the influence of moisture, latent heat release, and condensate transport on the vertical energy flux.

The flux decomposition used here follows the equivalent, or moist-static-energy, approach of Thomas et al. [50], who combine the temperature and water-vapour conservation equations into a single equivalent flux for cloudy Rayleigh–Bénard convection. The present formulation adopts the same idea but normalises every flux by the common dry conductive reference q_{ref} defined above, so that the resulting diagnostic is a dry-reference equivalent Nusselt number.

For the dry simulation, the relevant flux is the sensible heat flux,

$$\Phi_{\text{s}}(z) = \rho_g c_{p,g}\, \overline{w'T'} - \lambda_t \frac{\partial \overline{T}}{\partial z}, \tag{3.5}$$

where the first term is the turbulent convective heat flux and the second the diffusive (conductive) heat flux. Here w' and T' are fluctuations with respect to the horizontal mean, the overbar denotes horizontal averaging, ρ_g and $c_{p,g}$ are the gas density and specific heat, and $\lambda_t = \rho_g c_{p,g} \kappa_t$ is the effective thermal conductivity carried by the eddy diffusivity κ_t. The sensible Nusselt number is then

$$Nu_{\text{s}} = \frac{\Phi_{\text{s}}}{q_{\text{ref}}}. \tag{3.6}$$

In a purely conductive state the convective term vanishes and $\Phi_{\text{s}} \to \lambda_t\, \Delta T/H = q_{\text{ref}}$, so that $Nu_{\text{s}} \to 1$, recovering the classical normalisation.

In the moist case, water vapour transport introduces an additional latent-energy flux. The latent contribution is computed from the vapour mass-fraction field ξ as

$$\Phi_{\text{l}}(z) = \rho_g L_v\, \overline{w'\xi'} - \rho_g L_v D_t \frac{\partial \overline{\xi}}{\partial z}, \tag{3.7}$$

where the first term is the turbulent vertical transport of vapour and the second the diffusive vapour flux, both expressed in energy units through the latent heat L_v. The corresponding latent Nusselt number is

$$Nu_{\text{l}} = \frac{\Phi_{\text{l}}}{q_{\text{ref}}}. \tag{3.8}$$

The total moist energy transport is then measured using an equivalent, or moist-enthalpy, flux,

$$\Phi_{\mathrm{eq}}(z) = \Phi_{\mathrm{s}}(z) + \Phi_{\mathrm{l}}(z), \tag{3.9}$$

and the equivalent Nusselt number reported in the post-processing is

$$Nu_{\mathrm{eq}} = \frac{\Phi_{\mathrm{eq}}}{q_{\mathrm{ref}}} = \frac{\rho_g c_{p,g}\,\overline{w'T'} - \lambda_t \partial_z \overline{T} + \rho_g L_v\,\overline{w'\xi'} - \rho_g L_v D_t \partial_z \overline{\xi}}{\lambda_{\mathrm{ref}} \Delta T / H}. \tag{3.10}$$

This definition retains the sensible and latent components separately while providing a single total energy-transport measure for the moist run.

3.2 Dry Convection

The dry case (D1) provides the reference configuration against which the moist simulation is later compared. The flow is driven solely by the imposed wall temperature contrast—$T_{\text{bot}} = 295\,\text{K}$ at the lower wall and $T_{\text{top}} = 285\,\text{K}$ at the upper wall, giving $\Delta T = 10\,\text{K}$ about a mean temperature of $T_0 \approx 290\,\text{K}$—with phase change disabled, so that no latent heat is released and no condensate forms. The governing equations were integrated using a fixed time step of $\Delta t = 0.05\,\text{s}$, which satisfies the Courant–Friedrichs–Lewy (CFL) stability constraints associated with advection and diffusive transport. The analysis proceeds from the approach to a statistically steady state, through the large-scale organisation of the flow and its mean thermal structure, to the turbulent velocity statistics.

The organisation of the flow is illustrated in Figure 3.1, which shows the temperature field overlaid with instantaneous streamlines at successive times. At early times the flow is dominated by numerous small thermal plumes detaching from both walls. As the flow develops, these plumes merge and self-organise into a single domain-filling convection roll, consistent with the unit aspect ratio, in which warm fluid ascends on one side of the cell and cool fluid descends on the other. The roll persists over long times while slowly meandering, which is the characteristic large-scale circulation of confined Rayleigh–Bénard convection.

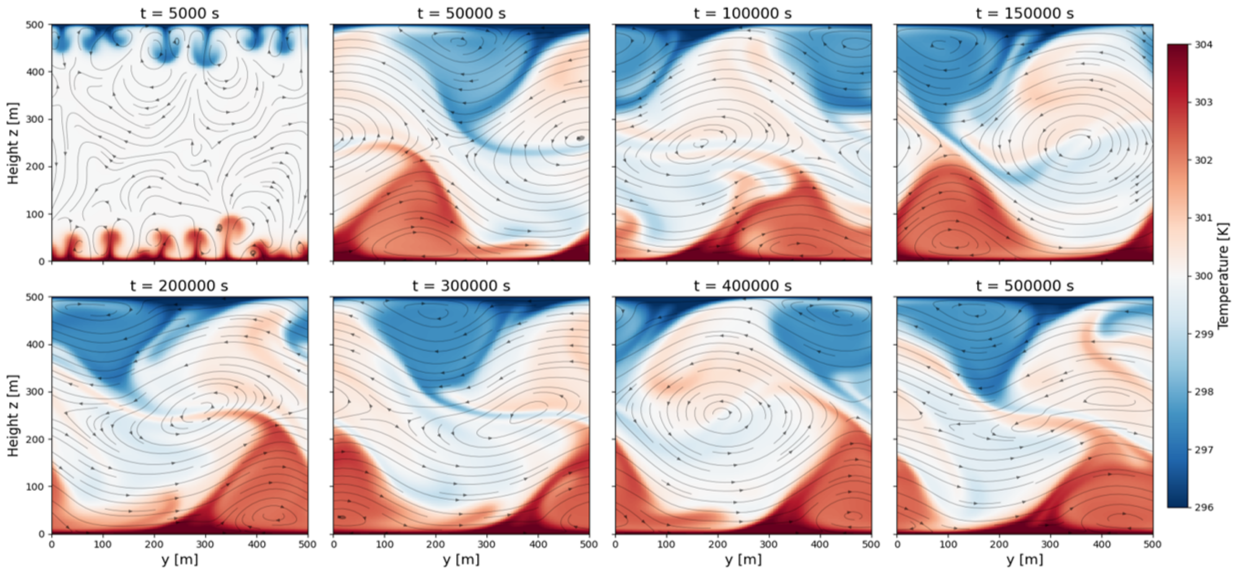

Figure 3.1: Temperature field with streamlines at successive times. Dry case

In transient numerical simulations of turbulent convection, the fluid is initially at rest and undergoes a chaotic "spin-up" phase as thermal instabilities develop and buoyancy forces begin to drive motion. During this initial period, the macroscopic properties of the flow are highly unbalanced and change rapidly.

To ensure that the data used for the thermodynamic and transport analysis is robust, it is first necessary to verify that the simulation has reached a statistically steady state—the regime in which the initial transient behaviour has decayed and global flow metrics oscillate around a stable, constant mean. To quantify the turbulent intensity and track this equilibrium, two fundamental global metrics are evaluated across the domain: the root-mean-square (RMS) velocity and the specific turbulent kinetic energy. The temporal evolution of these metrics for the dry reference case (D1) is presented in Figures 3.2 and 3.3.

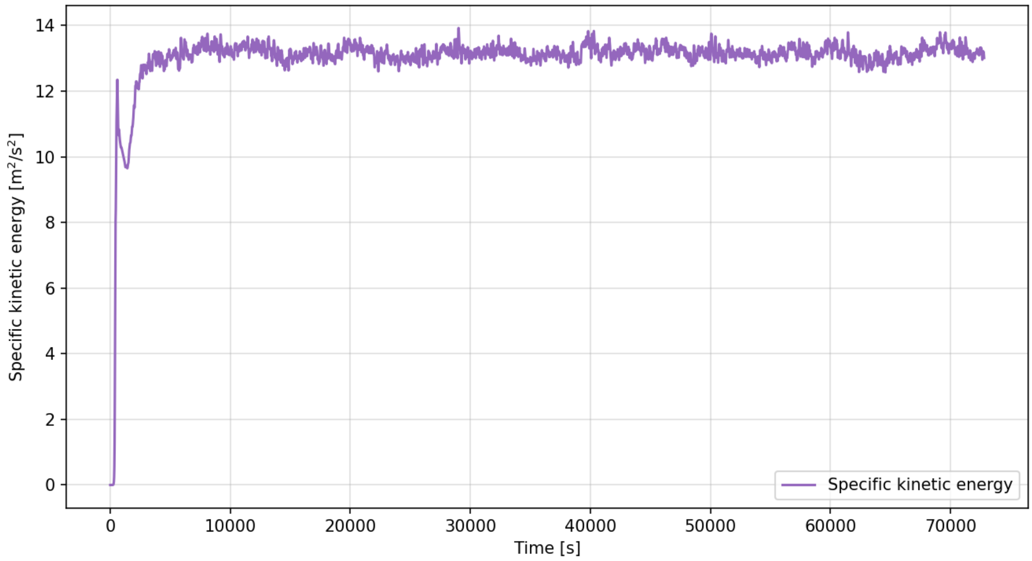

Figure 3.2: Time evolution of the averaged specific kinetic energy.Dry case

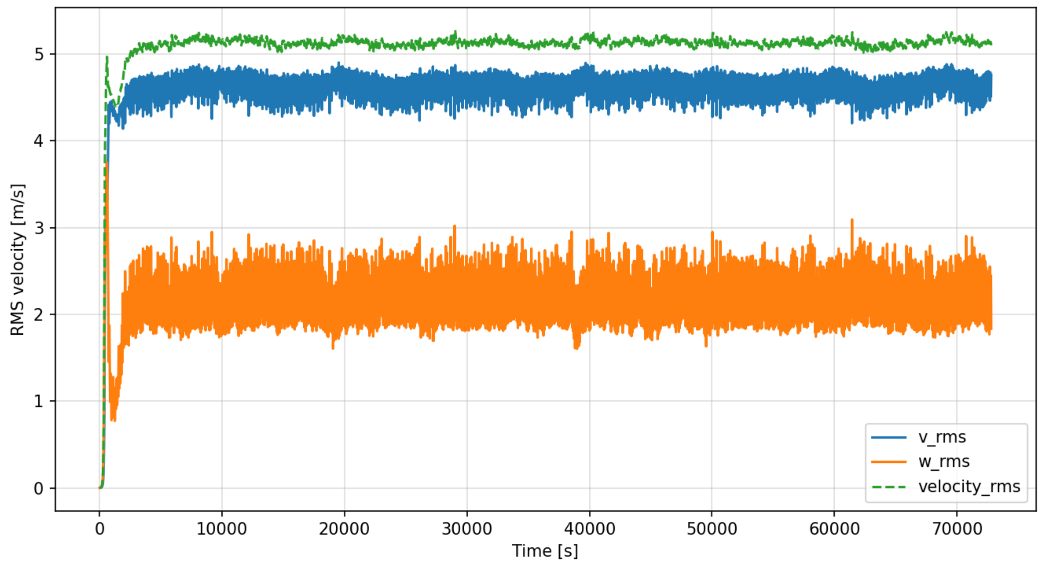

Figure 3.3: Time series of the RMS velocities. Dry case

Both figures demonstrate a consistent and stable turbulent regime. As shown in Figure 3.2, from $t = 0$ to roughly $t = 5000$ s the kinetic energy rises sharply as the imposed boundary temperatures break the fluid's initial resting state into convective plumes. After this transient the system reaches a statistically steady state: the specific kinetic energy levels off and maintains a tight oscillation around 13 m^2/s^2 for the remaining $\sim$65,000 s of the simulation, indicating that kinetic-energy production by buoyancy is statistically balanced by viscous dissipation within the domain. All subsequent time-averaged diagnostics (such as the Nusselt number calculations) are therefore evaluated over this $t > 5000$ s window.

The RMS velocity series (Figure 3.3) reveals the anisotropy of the established convection. In this 2D square domain ($\Gamma = 1$), the horizontal velocity ($v_{\text{rms}} \approx 4.6$ m/s) is distinctly stronger than the vertical velocity ($w_{\text{rms}} \approx 2.2$ m/s). This kinematic separation is characteristic of a domain-filling large-scale circulation cell: broad, coherent horizontal winds sweep along the top and bottom plates over a large fraction of the domain, while vertical transport is confined to comparatively narrow upwelling and downwelling thermal plumes. The two metrics are mutually consistent: using the fully developed total RMS velocity ($V_{\text{rms}} \approx 5.1$ m/s), the specific kinetic energy follows as $\frac{1}{2}V_{\text{rms}}^2 \approx \frac{1}{2}(5.1)^2 \approx 13.0$ m^2/s^2, in agreement with the explicit kinetic-energy diagnostic.

To quantify the total vertical energy transport in the dry reference simulation, the sensible Nusselt number was evaluated at the upper and lower boundaries. Because the velocity vanishes at the solid walls, the turbulent convective flux is zero there, and the total heat transport entering and exiting the domain can be extracted directly from the conductive wall gradients.

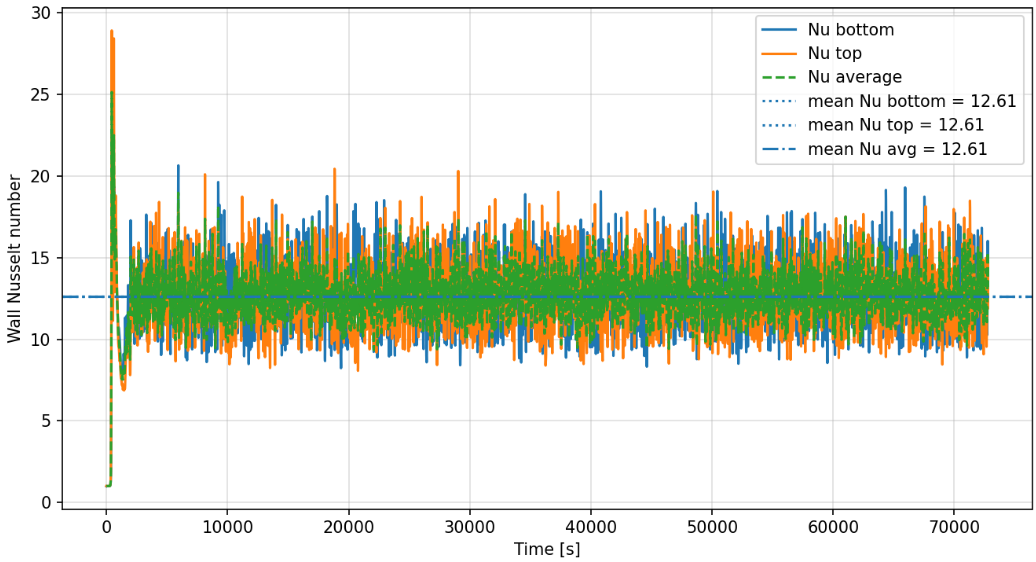

Figure 3.4: Time series of the wall Nusselt number plates. Dry case

As shown in Figure 3.4, following the initial transient spin-up the heat-transfer efficiency reaches a statistically steady state, with the mean Nusselt number stabilising at $Nu_s = 12.61$, indicating that the buoyancy-driven overturning transports roughly twelve times more heat than a purely conductive, stagnant fluid. The agreement between the top and bottom wall Nusselt numbers, within statistical fluctuations, confirms that the heat entering through the lower wall is balanced by the heat leaving through the upper wall, so that the net vertical heat flux is conserved across the domain.

While the wall Nusselt number confirms the global energy balance at the boundaries, the vertical profile of the flux provides insight into the internal transport mechanics. As defined in Eq. (3.5), the total sensible heat flux, $\Phi_s(z)$, is the sum of the turbulent convective and the diffusive (conductive) heat fluxes, whose time-averaged vertical profiles for the dry reference case are presented in Figure 3.5.

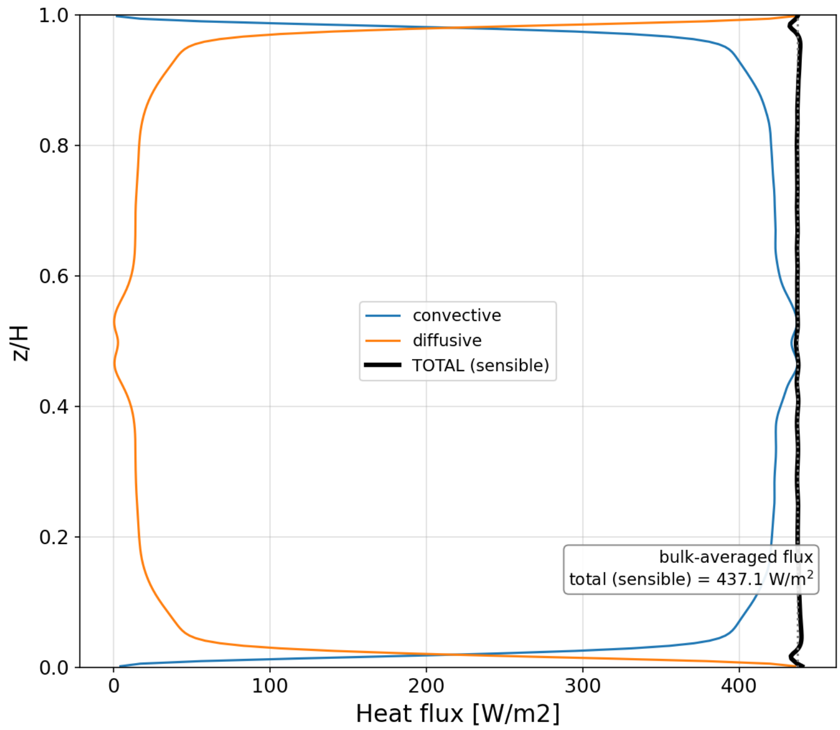

Figure 3.5: Time-averaged vertical profiles of the heat fluxes. Dry case.

The vertical partitioning clearly demonstrates the boundary-layer dynamics of the system. In the bulk interior, heat transport is overwhelmingly dominated by the turbulent convective flux. As the flow approaches the impermeable top and bottom walls, however, the vertical velocity vanishes due to the kinematic boundary conditions, so the convective flux decays to zero and the diffusive flux increases sharply to maintain the transport of energy through the thin near-wall layers.

The sum of these two components—the total sensible heat flux—remains nearly constant across the entire height of the domain at approximately 434 W/m^2 (consistent with $Nu_s \times q_{\mathrm{ref}}$). This uniform vertical profile is a direct consequence of energy conservation in a statistically steady state: with no internal heat sources, the flux entering the lower wall must equal that leaving the upper wall at every height. Its flatness therefore confirms both the convergence of the averaging window and the internal consistency of the convective–diffusive decomposition.

The vertical structure of the convective layer could be characterized by the time-averaged profiles of temperature, water-vapor mass fraction, and relative humidity (RH), as shown in Figures 3.6 and 3.7.

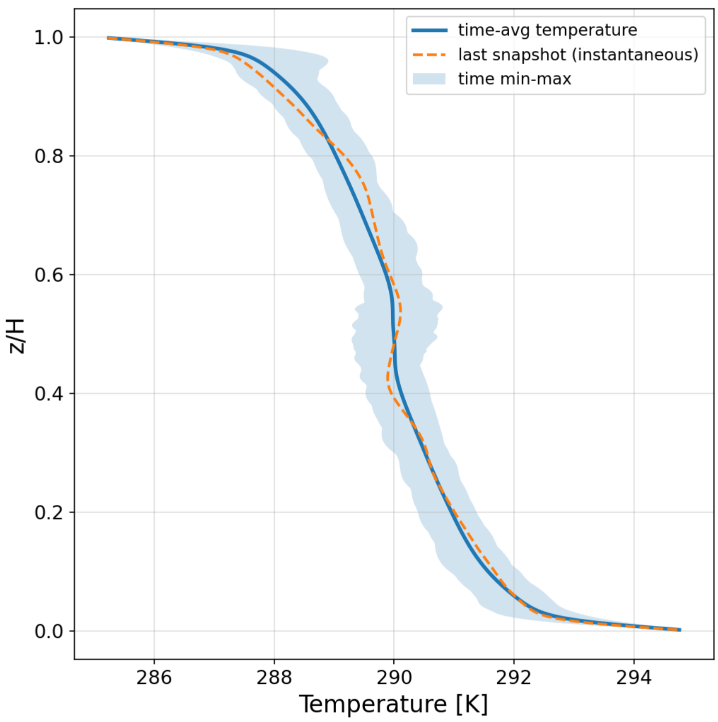

Figure 3.6: Time-averaged vertical temperature profile. Dry case

As seen in Figure 3.6, the initial linear temperature gradient is rapidly flattened by turbulent overturning, resulting in a nearly isothermal bulk region between $0.2 < z/H < 0.8$ pinned at the mean wall temperature $T_0 \approx 290\,\mathrm{K}$, with steep gradients confined to thin thermal boundary layers at each wall. Because almost the entire temperature contrast is sustained across these thin layers rather than the interior, the convective heat transport is strongly enhanced relative to conduction ($Nu_\mathrm{s} > 1$).

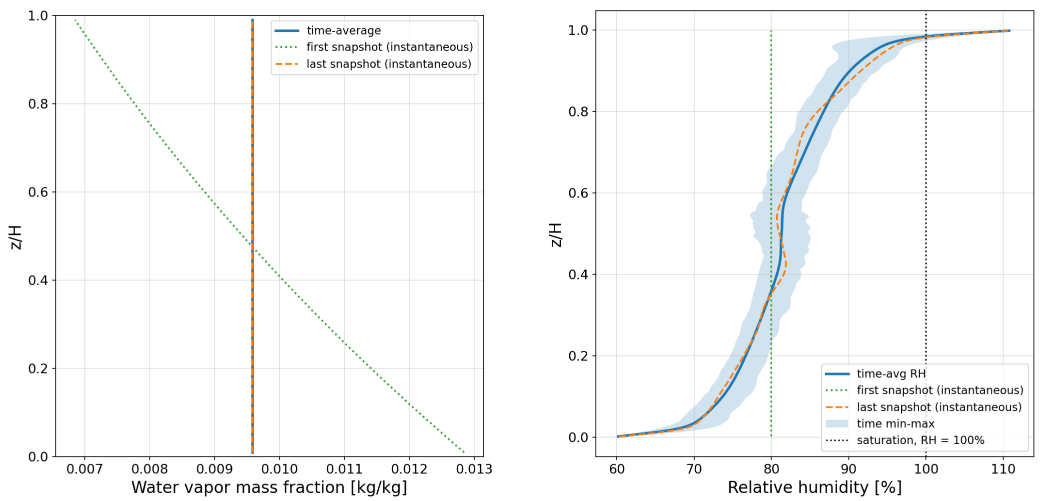

Figure 3.7: Time-averaged vertical profiles of the water-vapour mass fraction (left) and relative humidity (right). Dry Case

Because phase change is disabled in D1, the water vapour behaves as a passive scalar, providing a further check on the flow. As shown in Figure 3.7 (left), turbulent mixing erases the initial linear mass-fraction gradient and drives the vapour towards a vertically uniform value, $\xi \approx 9.6 \times 10^{-3}$, equal to the vertical average of the initial distribution—direct evidence of complete turbulent mixing. With the mean profile uniform and the walls impermeable to moisture, the net vertical vapour flux vanishes, so the dry-case energy transport is carried entirely by sensible heat and is characterised completely by Nu_s.

A notable feature of the relative-humidity profile (Figure 3.7, right) is that, although the vapour mass fraction is uniform, the relative humidity increases monotonically with height, approaching saturation (RH $\approx$ 100%) near the cold upper plate. This follows directly from RH $= \xi/\xi_\mathrm{sat}(T)$: as ξ_sat falls with the temperature, a uniform vapour field yields a humidity that rises towards the top, and since condensation is disabled the flow can locally reach or slightly exceed saturation without forming liquid water. This identifies the upper region as where phase change would first be triggered once the moist coupling is activated, directly motivating the moist case (M1) examined next.

Figure 3.8 presents the vertical profiles of the horizontal and vertical velocity variances in the statistically stationary dry regime. Beyond the velocity RMS, the variances reveal how the turbulent kinetic energy is distributed among the components and varies with height, offering insight into its production, redistribution, and transport within the convective layer.

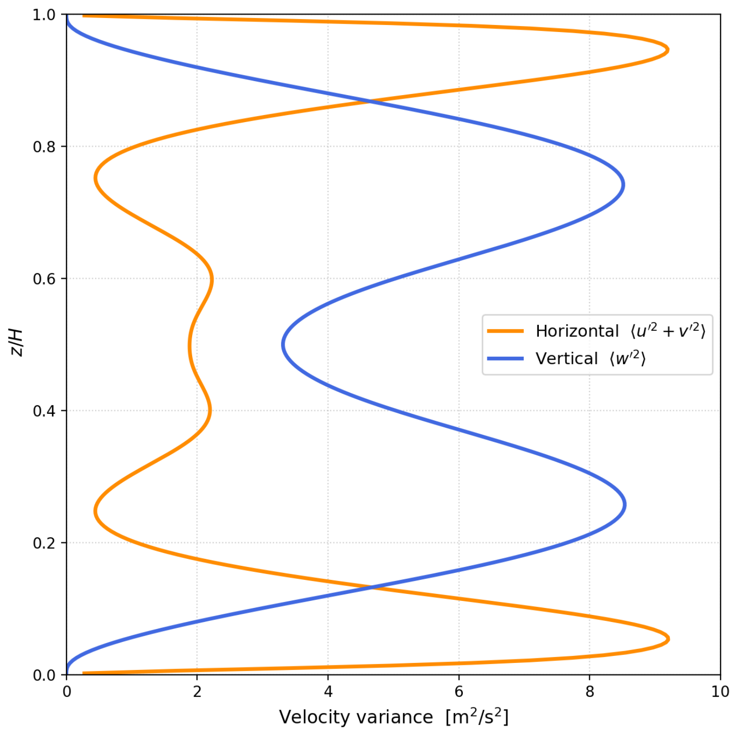

Figure 3.8: Vertical profiles of the velocity variances. Dry Case.

The vertical velocity variance, $\langle w'^2 \rangle$, exhibits two pronounced maxima away from the boundaries, at approximately $z/H \approx 0.25$ and 0.75. These correspond to the locations where buoyancy-driven thermal plumes detach from the thermal boundary layers and accelerate into the interior. As expected from the no-slip and impermeability boundary conditions, the vertical variance decreases towards zero at both plates, where vertical motion is prohibited.

In contrast, the horizontal velocity variance, reaches its largest values near the upper and lower boundaries, a consequence of plume impingement at the walls. When rising hot plumes reach the cold upper plate, or descending cold plumes reach the warm lower plate, their vertical motion is arrested and redirected into horizontal flow along the boundary. The resulting lateral spreading enhances the horizontal velocity fluctuations close to the walls and produces the observed variance maxima.

The staggered locations of the horizontal and vertical variance peaks highlight the strongly anisotropic nature of the flow. Buoyancy primarily generates vertical motions in the plume-acceleration regions, and part of this kinetic energy is subsequently transferred into horizontal motions through plume–wall interactions and the large-scale circulation. The variance profiles therefore illustrate the continuous redistribution of turbulent kinetic energy between the vertical and horizontal components that characterises two-dimensional Rayleigh–Bénard convection.

Taken together, these diagnostics confirm that the dry case reproduces the expected phenomenology of turbulent Rayleigh–Bénard convection—a well-mixed core bounded by thin thermal and viscous boundary layers, a nearly height-independent heat flux, plume-dominated velocity statistics, and an organised large-scale circulation—and therefore provides a reliable, well-converged baseline for the moist comparison presented in the following section.

3.3 Moist Convection

We now turn to the central configuration of this work: moist convection with phase change, commonly referred to as cloudy Rayleigh–Bénard convection, in which both the lower and upper plates are maintained at saturation (RH = 100%). The warm lower plate (295 K) and the cold upper plate (285 K) impose saturated water-vapour boundary conditions, so that the air adjacent to each wall carries the saturation vapour content corresponding to the local wall temperature. The saturation vapour concentration is evaluated from the Antoine equation, whose strong temperature dependence reflects the Clausius–Clapeyron relation; as a result, the warmer lower plate supports roughly twice the water-vapour content of the colder upper plate, establishing a vertical moisture gradient across the layer.

To isolate the effects of moisture and phase change, the moist case (M1) employs exactly the same geometry, numerical resolution, and governing dimensionless parameters as the dry reference case (D1). In particular, the domain dimensions, temperature difference, and resulting Rayleigh number ($Ra \approx 3.0 \times 10^7$), together with the turbulent Prandtl and Schmidt numbers ($\mathrm{Pr}_t = 0.7$ and $\mathrm{Sc}_t = 0.6$), are identical in both simulations. The moist case therefore differs from the dry reference only through the introduction of water vapour, condensation, latent heat release, and precipitation. Any differences in the resulting flow behaviour can thus be attributed directly to the moist physics rather than to changes in the flow configuration.

The moist model introduces several additional parameters that govern the phase-change and precipitation processes:

- a condensation relaxation time, $\tau_c \approx 388\,\mathrm{s}$ ($\tau_c^{-1} = 2.58 \times 10^{-3}\,\mathrm{s}^{-1}$), which controls the rate at which supersaturated vapour is converted into liquid water and sets the Damköhler number, $Da \approx 0.10$;
- a constant terminal settling velocity for cloud liquid water, $w_{\mathrm{set}} = 8\,\mathrm{m\,s}^{-1}$, corresponding to a Rouse number $Ro = w_{\mathrm{set}}/U_0 \approx 0.62$;
- a rain-activation threshold, $\alpha_{1,c} = 5 \times 10^{-7}$, above which liquid water is permitted to settle and precipitate toward the lower boundary. This plays the role of the cloud-water threshold in Kessler-type autoconversion [61]: below it the condensate remains suspended and moves with the flow, while above it it is large enough to fall under gravity. The threshold is set roughly an order of magnitude below the peak liquid fraction reached in the simulation, so that dense condensate cores precipitate while thin, dilute regions remain suspended.

Together, these parameters determine how water vapour condenses into cloud liquid water, how the resulting condensate settles under gravity, and how it is ultimately removed from the system as precipitation.

The governing equations were integrated using a fixed time step of $\Delta t = 0.01\,\mathrm{s}$, an order of magnitude smaller than in the dry case. This value resolves the phase-change relaxation timescale while satisfying the Courant–Friedrichs–Lewy (CFL) stability constraints associated with advection, momentum transport, and the diffusion of heat and moisture, ensuring a stable and accurate coupling between turbulent transport, latent heating, and condensation.

An important aspect of reaching a stationary moist state is the treatment of condensed liquid water at the lower boundary. Once settling liquid water reaches the bottom of the domain it is removed from the system and interpreted as rain. This prevents the indefinite accumulation of water and allows the system to equilibrate: the vapour supplied through the saturated boundaries is balanced by the liquid water removed through precipitation, so that the total water content fluctuates around a nearly constant mean.

The saturated-plate configuration is the moist counterpart of the classical dry Rayleigh–Bénard problem and is closely related to the canonical cloudy-convection setup studied by Thomas et al. [50]. It provides a simple yet physically meaningful framework for investigating the interaction between buoyancy-driven turbulence, phase change, latent heat release, and precipitation. The choice of saturated boundaries is also motivated by its relevance to atmospheric cloud layers, which often develop between humid lower regions that continuously supply moisture and upper regions that remain close to saturation. Imposing saturation at both plates idealises this situation and provides a persistent source of water vapour capable of sustaining cloud formation throughout the domain. As air parcels rise they cool, frequently reaching supersaturation and condensing; the associated latent heat release locally warms the air, enhances buoyancy, and modifies the convective motion. Through this mechanism moisture participates actively in the dynamics rather than behaving as a passive scalar, in contrast to the dry case.

This configuration therefore provides a controlled environment in which the effects of condensation, latent heating, cloud formation, and precipitation can be investigated systematically. The remainder of this section examines the evolution toward statistical steady state, the closure of the water budget, the vertical structure of temperature and moisture, the distribution of cloud liquid water, and the partitioning of the vertical energy transport between sensible and latent contributions.

Because moisture is continuously supplied at the saturated plates and removed only through precipitation at the lower boundary, the closure of the water budget provides the primary indicator of statistical stationarity for the moist case. Unlike the velocity field, whose equilibration is examined separately below, the domain-wide moisture content equilibrates slowly, since it is governed by the condensation and precipitation cycle—the balance between vapour supplied at the walls and liquid removed as rain—rather than by the convective spin-up. Figure 3.9 shows the time evolution of the total water, water-vapour, and liquid-water inventories in the domain.

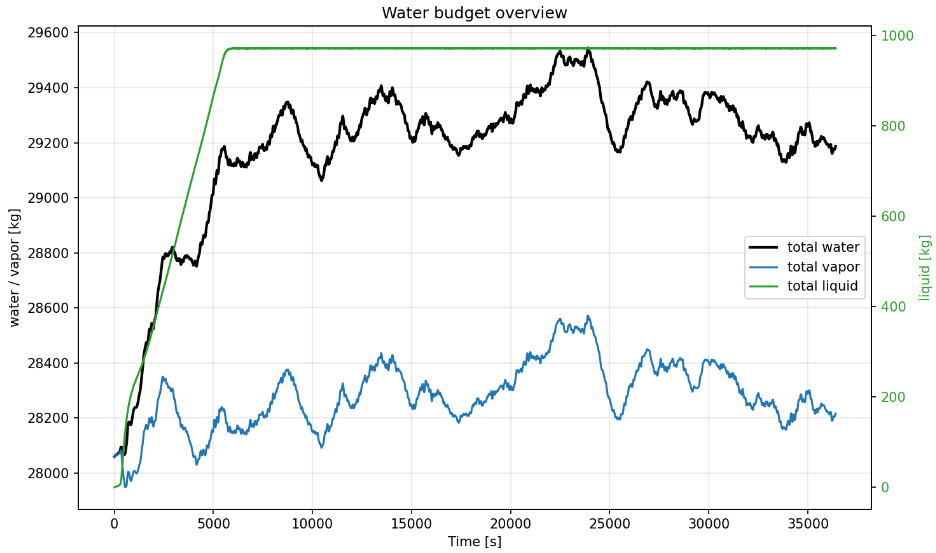

Figure 3.9: Time evolution of the total water. Moist case

Following the initial transient, the liquid-water inventory rises steeply as condensation switches on and then saturates at a nearly constant value once precipitation begins to remove liquid at the lower boundary, at approximately $t \approx 5500\,\mathrm{s}$. Thereafter the total water and vapour inventories fluctuate around stable mean values without systematic drift, indicating that the moisture supplied through the saturated plates is balanced, on average, by the liquid water removed as rain. The closure of this budget confirms that the simulation has reached a fully developed statistically stationary regime, and all subsequent time-averaged diagnostics are evaluated over this window.

The turbulent intensity reaches equilibrium on a shorter timescale, as shown by the RMS velocity series in Figure 3.10. After the spin-up the horizontal (v_{rms}), vertical (w_{rms}), and total (V_{rms}) RMS velocities settle to statistically steady values. The total RMS velocity, $V_{\mathrm{rms}} \approx 5.7\,\mathrm{m\,s^{-1}}$, exceeds the dry-case value ($\approx 5.1\,\mathrm{m\,s^{-1}}$), a first indication that the release of latent heat energises the convective motion relative to the dry reference.

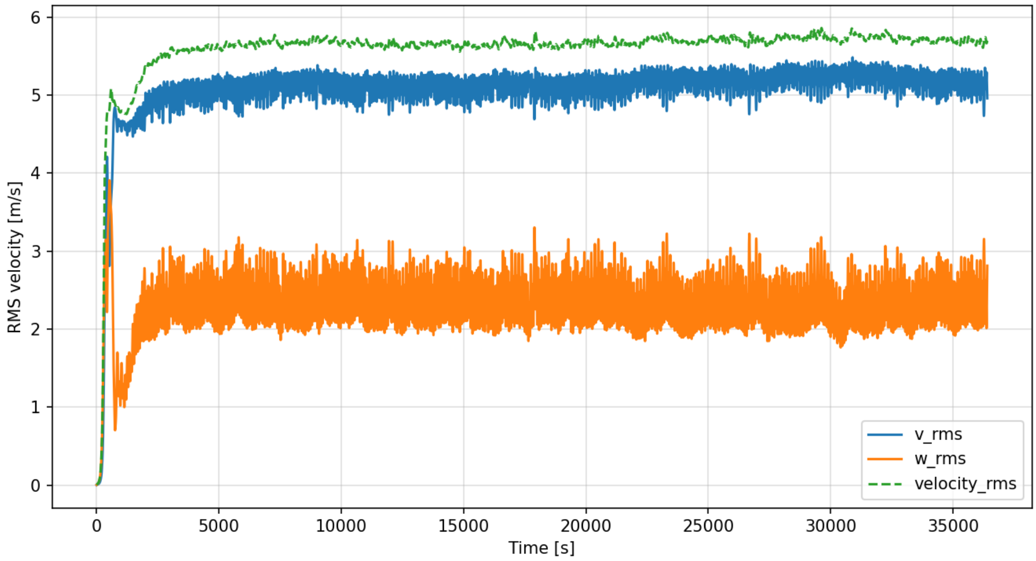

Figure 3.10: Time series of the RMS velocities. Moist case

The time-averaged vertical temperature profile is shown in Figure 3.11. Its overall shape follows the structure seen in the dry case—steep thermal gradients confined to thin boundary layers at each plate, enclosing a well-mixed core. The key difference lies in the bulk: whereas the dry interior is nearly isothermal and pinned at the mean wall temperature $T_0 \approx 290\,\mathrm{K}$, the moist core is slightly warmer. This warming and stabilisation are the signature of latent heating: as saturated air rises and cools, condensation releases latent heat into the interior, warming it relative to the lower layers and partially offsetting the imposed unstable gradient.

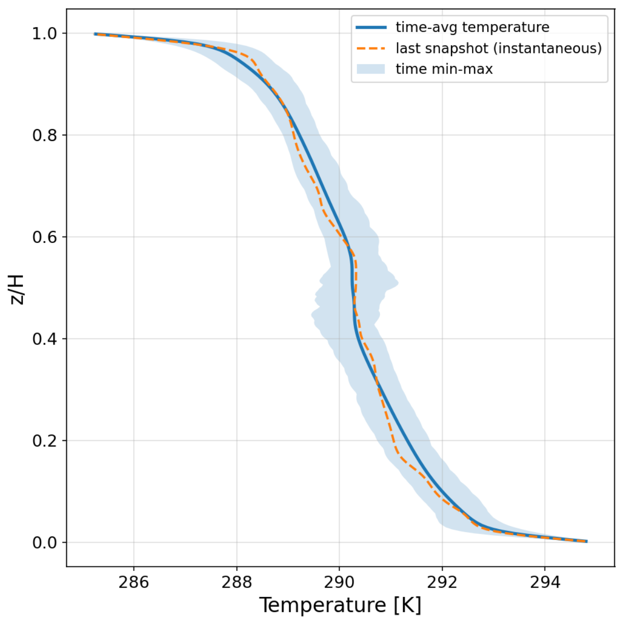

Figure 3.11: Time-averaged vertical temperature profile. Moist case

The moisture fields are shown in Figure 3.12. The water-vapour mass fraction (left) decreases monotonically with height, from $\approx 1.5 \times 10^{-2}$ near the warm lower plate to $\approx 9 \times 10^{-3}$ near the cold upper plate, following the saturation gradient imposed by the Clausius–Clapeyron dependence of the wall boundary conditions. Unlike the dry case, in which the vapour was homogenised into a uniform profile, here the active condensation and the saturated boundaries maintain a persistent vertical vapour gradient. The liquid-water mixing ratio (right) is nearly uniform with height at $\approx 0.41\,\mathrm{g\,kg^{-1}}$, indicating that cloud water is present throughout the entire depth of the domain rather than confined to a discrete cloud layer, consistent with the fully saturated configuration.

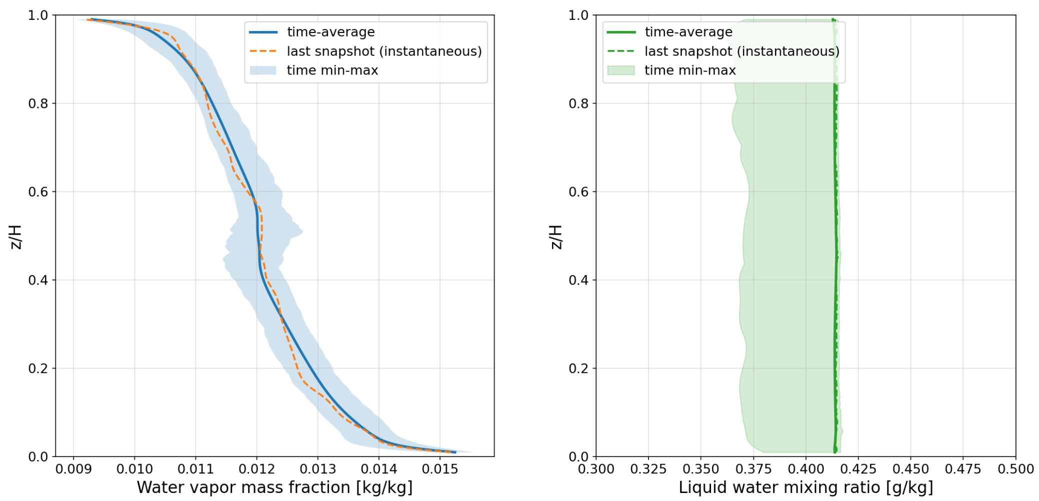

Figure 3.12: vertical profiles of the water-vapour mass fraction (left) and liquid-water mixing ratio (right). Moist case

Both moisture profiles and the temperature profile display a common inflection near mid-height ($z/H \approx 0.5$), where the temporal fluctuation envelope is also broadest. This coincides with the core of the large-scale circulation, where the rising and descending branches meet and the strongest condensation and evaporation occur.

The central diagnostic of the moist case is the partitioning of the vertical energy transport between its sensible and latent components. The time-averaged decomposition of the convective fluxes is shown in Figure 3.13, and the full equivalent-flux budget, including the diffusive contributions, in Figure 3.14.

As shown in Figure 3.13, the convective latent flux—the turbulent vapour-transport term $\rho_g L_v\,\overline{w'\xi'}$ of Eq. (3.7), $\approx 870\,\mathrm{W\,m^{-2}}$ in the bulk—is nearly twice the convective sensible flux $\rho_g c_{p,g}\,\overline{w'T'}$ of Eq. (3.5), $\approx 460\,\mathrm{W\,m^{-2}}$. The transport of energy in the moist case is therefore dominated by the latent contribution.

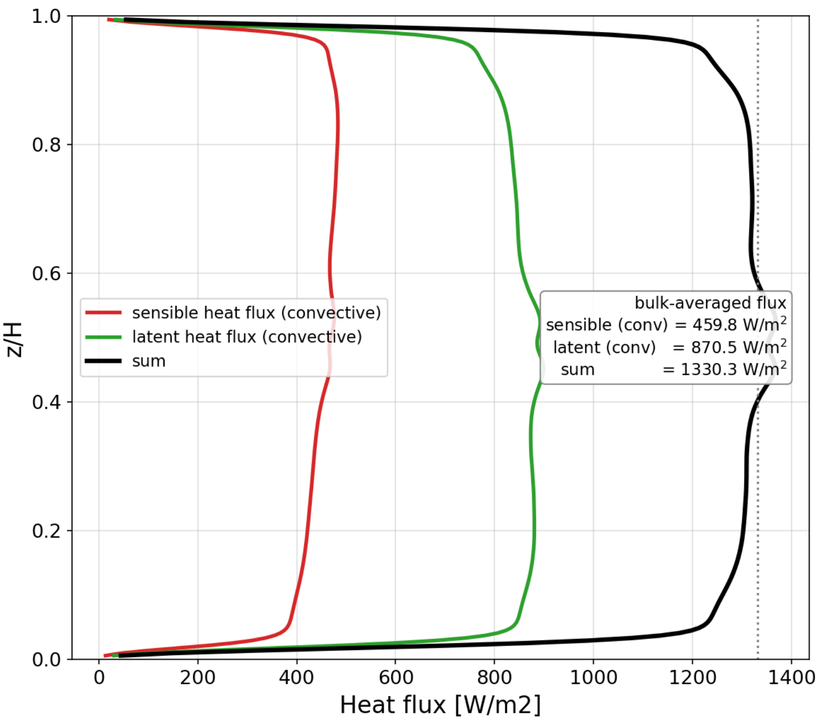

Figure 3.13: Vertical profiles of the convective sensible and latent heat fluxes.

Physically, the latent flux measures energy carried not as a temperature excess but as water vapour: buoyant parcels rising from the warm lower plate carry a high vapour content upward, giving a positive correlation $\overline{w'\xi'} > 0$, and release this energy as latent heat when they cool and condense aloft, while descending subsaturated parcels re-evaporate liquid and carry the deficit downward. Vapour thus acts as an energy carrier that is loaded at the base of an updraught and released higher up, so that even a modest turbulent mass flux of water conveys a large energy flux through the latent heat L_v. Both convective fluxes vanish at the walls, where the vertical velocity is zero, and their sum is nearly height-independent through the interior.

This latent pathway is precisely the mechanism by which the real atmosphere accomplishes much of its vertical energy transport. In moist atmospheric convection, energy is carried from the surface to the upper troposphere predominantly as the latent heat of water vapour, which is released upon condensation to drive clouds and storms and to couple the hydrological cycle to the atmospheric energy budget. The dominance of the latent over the sensible flux found here is therefore the idealised counterpart of this atmospheric behaviour, and it is the direct consequence of allowing phase change that the dry reference case, by construction, cannot reproduce.

The complete equivalent-flux budget is shown in Figure 3.14, which separates each of the sensible and latent contributions into convective and diffusive parts. Each flux is the sum of a turbulent convective term and a diffusive term: for the sensible flux these are $\rho_g c_{p,g}\,\overline{w'T'}$ and $-\lambda_t\,\partial_z\overline{T}$ (Eq. (3.5)), and for the latent flux the corresponding vapour terms $\rho_g L_v\,\overline{w'\xi'}$ and $-\rho_g L_v D_t\,\partial_z\overline{\xi}$ (Eq. (3.7)). As in the dry case, the diffusive contributions—negligible in the well-mixed interior—dominate within the thin boundary layers, where the vanishing vertical velocity suppresses the convective terms and transport is sustained by the mean gradients of temperature and vapour; the convective terms dominate the bulk, and the two hand over smoothly across the near-wall region. Crucially, the equivalent (moist-static-energy) flux—the sum of all four contributions, Eq. (3.9)—is constant with height across the entire domain at $\approx 1368\,\mathrm{W\,m^{-2}}$, confirming energy conservation in the moist statistically stationary state.

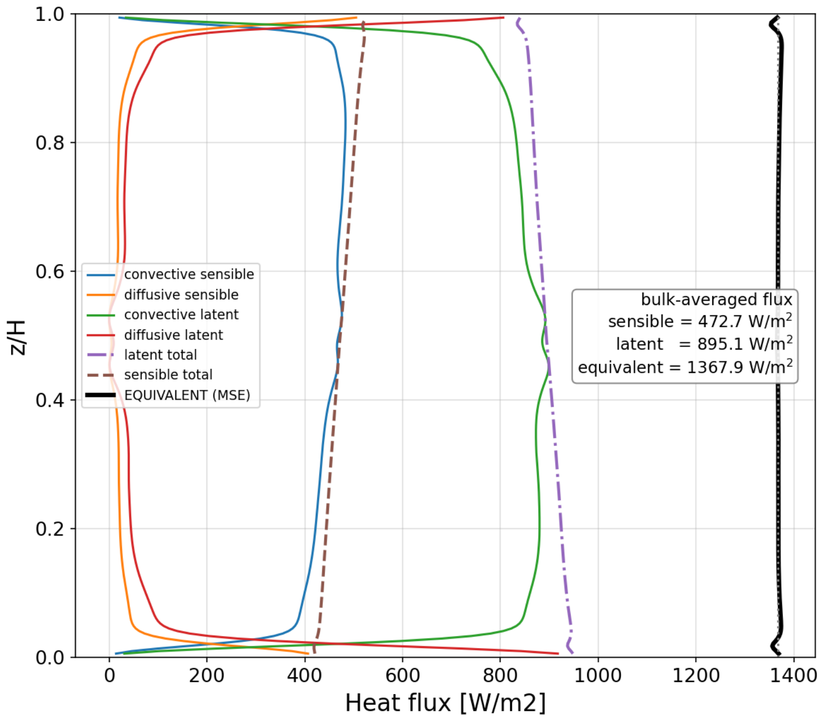

Figure 3.14: Vertical profiles of the heat fluxes. Moist case

Normalising the bulk equivalent flux by the same dry reference flux $q_{\mathrm{ref}} \approx 34.4\,\mathrm{W\,m^{-2}}$ used throughout, Eq. (3.10), gives an equivalent Nusselt number of $Nu_{\mathrm{eq}} \approx 40$, compared with $Nu_{\mathrm{s}} \approx 12.6$ for the dry case. Decomposing the moist value into its two channels, the sensible Nusselt number, Eq. (3.6), is $Nu_{\mathrm{s}} \approx 13.7$, only marginally above the dry value, whereas the latent Nusselt number, Eq. (3.8), is $Nu_{\mathrm{l}} \approx 26$, roughly twice as large. The sensible transport is therefore only slightly enhanced by the presence of moisture, while essentially all of the additional energy transport is supplied through the latent pathway that is absent in the dry reference. On a common basis, the moist configuration transports roughly three times more energy than the dry case. This quantifies a central result of this work: phase change fundamentally alters the efficiency of the convective heat engine.

Finally, the vertical profiles of the horizontal and vertical velocity variances are shown in Figure 3.15. The structure mirrors the dry case—a double-lobed vertical variance with maxima near $z/H \approx 0.25$ and 0.75, marking plume detachment, and horizontal variance peaking near the walls where plumes impinge—but the magnitudes are larger, the vertical variance reaching $\approx 11\,\mathrm{m^2\,s^{-2}}$ against $\approx 8.5\,\mathrm{m^2\,s^{-2}}$

in the dry case. This enhancement is the kinematic counterpart of the latent-heat energisation already seen in the RMS velocities: condensation within ascending plumes adds buoyancy and accelerates the vertical motion, strengthening the plume-driven fluctuations relative to the dry reference.

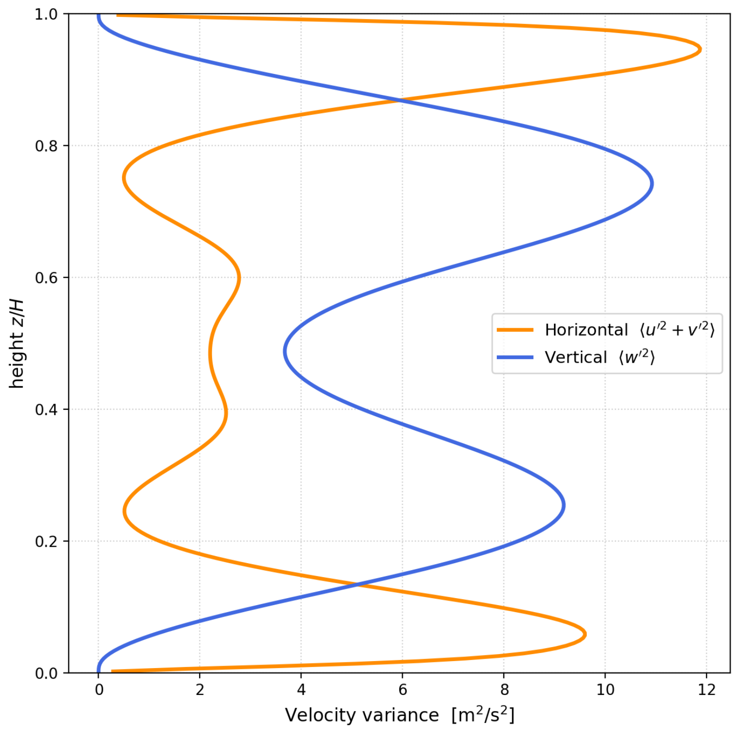

Figure 3.15: Vertical profiles of velocity variances. Moist case

Taken together, these diagnostics show that the introduction of phase change, while preserving the overall large-scale organisation of the flow, substantially intensifies the convection and shifts the dominant mode of vertical energy transport from sensible to latent heat, establishing the moist case as a qualitatively distinct convective regime from the dry reference.

Chapter 4

Conclusions and Future Work

4.1 Conclusions

This thesis investigated moist atmospheric convection with phase change through numerical simulation of an idealised cloudy Rayleigh–Bénard configuration. A two-phase Boussinesq mixture model with a relaxation-based phase-change closure was employed to simulate a $500 \times 500\,\mathrm{m}$ vertical layer driven by a $10\,\mathrm{K}$ wall temperature contrast, at an effective turbulent Rayleigh number of $Ra \approx 3 \times 10^7$. Two simulations were carried out on identical grids and with identical dimensionless parameters: a dry reference case (D1), in which water vapour is carried as a passive scalar with phase change disabled, and a moist case (M1), in which both plates are held at saturation and condensation, latent heat release, condensate settling, and precipitation are active. Because the two cases differ only in the moist physics, their comparison isolates the effect of phase change on turbulent convective transport.

The dry reference case reproduces the established phenomenology of turbulent Rayleigh–Bénard convection: a well-mixed, nearly isothermal core bounded by thin thermal boundary layers, a single domain-filling large-scale circulation, plume-dominated velocity statistics, and a height-independent total heat flux. The sensible Nusselt number, evaluated consistently from the wall gradients and from the vertical flux profile, converges to $Nu_\mathrm{s} \approx 12.6$, and the vapour field is homogenised into a uniform vertical profile, confirming its passive character. These results establish D1 as a reliable, well-converged baseline and validate the numerical framework against classical expectations.

The central result of this work concerns the moist case. When phase change is activated, the vertical energy transport increases dramatically: the equivalent (moist-static-energy) flux reaches $\approx 1368\,\mathrm{W\,m^{-2}}$, compared with $\approx 434\,\mathrm{W\,m^{-2}}$ in the dry case. Referred to the same dry conductive reference flux, this corresponds to an equivalent Nusselt number of $Nu_\mathrm{eq} \approx 40$ against $Nu_\mathrm{s} \approx 12.6$—roughly a threefold enhancement of the total transport on a common basis. The decomposition of the flux shows that this enhancement is supplied almost entirely by the latent contribution: in the bulk, the convective latent heat flux ($\approx 870\,\mathrm{W\,m^{-2}}$) is nearly twice the convective sensible flux ($\approx 460\,\mathrm{W\,m^{-2}}$). Energy in the moist system is therefore transported primarily in the form of latent heat carried by water vapour, which condenses in ascending parcels and evaporates in descending ones, rather than by the direct transport of sensible heat.

The reason the moist Nusselt number is so much larger is physical rather than kinematic. The same overturning circulation that carries sensible heat also carries water vapour, and each unit of vapour transports an energy content $L_v\xi$ that greatly exceeds the sensible-heat content c_pT' associated with the typical temperature fluctuations. Phase change effectively opens a second, more efficient channel for vertical energy transport through the same turbulent motions. In addition, the latent heat released by condensation within rising plumes locally increases their buoyancy, intensifying the convection itself: the total RMS velocity increases from ≈ 5.1 to $\approx 5.7\,\mathrm{m\,s^{-1}}$ relative to the dry case. Latent heating therefore plays a dual role: it provides an additional pathway for vertical energy transport and, at the same time, an extra source of buoyancy that drives the flow more strongly. Yet it does not change the overall structure of the convection—the single large-scale circulation roll and the thin boundary layers at the walls remain the same as in the dry case; only their intensity increases.

The influence of phase change is not confined to the vertical motion. In the moist case, condensation releases latent heat in rising saturated regions, increasing buoyancy and strengthening the updraughts. The kinetic energy generated in this way is continuously redistributed between the velocity components: rising plumes are arrested at the upper plate and deflected into horizontal motion, and descending motions are similarly redirected near the lower plate. Consistent with this, the latent energisation of the convection also strengthens the horizontal winds, particularly in the near-wall regions where the large-scale circulation sweeps along the boundaries. The velocity-variance profiles support this picture. In the dry reference the two components are nearly symmetric about mid-height: the vertical variance peaks at $\approx 8.5\,\mathrm{m^2\,s^{-2}}$ at its two interior lobes ($z/H \approx 0.25$ and 0.75), and the horizontal variance reaches $\approx 9\,\mathrm{m^2\,s^{-2}}$ near both plates. In the moist case these maxima grow and become top-heavy: the vertical variance rises to ≈ 9.2 and $\approx 11\,\mathrm{m^2\,s^{-2}}$ at the lower and upper lobes, and the horizontal variance to ≈ 9.6 near the lower plate and $\approx 11.8\,\mathrm{m^2\,s^{-2}}$ near the upper plate. Both components are therefore enhanced by the latent energisation, and the concentration of that enhancement in the upper part of the layer is consistent with condensation and latent-heat release being strongest where the rising air cools to saturation.

The quantitative importance of the latent pathway is the principal reason this class of model is valuable. In the atmosphere, latent heat release is the dominant energy source of moist convection, and its representation is among the largest sources of uncertainty in weather and climate models. The present configuration reduces the problem to its essential ingredients—buoyancy-driven turbulence, a saturation constraint, a finite condensation timescale, and a simple precipitation sink—within a framework in which the energy budget can be closed exactly. The height-independence of the equivalent flux and the closure of the water budget, with the vapour supplied at the saturated plates balanced by the liquid removed as rain, demonstrate that the model conserves energy and water simultaneously in a statistically stationary state. This makes it a controlled environment in which the coupling between phase change and turbulence can be quantified cleanly, in a way that is not possible in more complex atmospheric models where many processes act at once.

4.2 Future Work

Several extensions of the present model would increase its physical realism and broaden the range of questions it can address.

The most direct extension follows from the results themselves and concerns the thermodynamic role of evaporation. In the current saturated configuration, the dominant moist feedback is condensation and latent-heat release in the updraughts. In more realistic unsaturated regions, and especially in the presence of falling rain, evaporation produces the opposite thermodynamic effect: latent heat is absorbed from the air, cooling it, increasing the negative buoyancy of descending parcels, and thereby strengthening the downdraughts. On reaching the lower region, this cold, dense air is deflected into horizontal outflow and modifies the near-surface wind—the mechanism that, in the atmosphere, underlies cold-pool formation and the spreading gust fronts that can in turn trigger new convection. The effect should be most pronounced where the vertical transport of water vapour is largest, since a greater moisture flux feeds both condensation in the ascending saturated regions and evaporation in the descending subsaturated ones. In the present idealised setup this evaporative pathway is only partially represented, because the lower plate is held at a fixed temperature and liquid is removed as rain at the boundary rather than allowed to accumulate; isolating this evaporative, cold-pool side of the feedback would require relaxing these boundary conditions.

A further extension concerns the cloud microphysics, which is treated here in a deliberately minimal form: all condensate is described by a single liquid field with one prescribed settling velocity, and precipitation is represented by a threshold-based removal at the lower boundary. A more precise treatment would distinguish between the two physically distinct categories of condensed water. Cloud water consists of small droplets whose settling velocity is negligible on convective timescales and which are effectively advected with the flow, whereas rain water consists of much larger drops that fall rapidly relative to the air. A two-category formulation would introduce a separate transport equation for each species: a cloud-water equation, in which the condensate moves essentially with the gas velocity, and a rain-water equation, in which the drops fall with their own, substantially larger terminal velocity. The conversion between the two categories (autoconversion of cloud water to rain, and accretion of cloud droplets by falling rain) would then be modelled explicitly, replacing the present single threshold. Assigning distinct velocities to the two species would also allow the momentum exchange between the falling rain and the surrounding air—the drag exerted by precipitation on the flow—to be captured, an effect that is entirely absent when a single settling velocity is prescribed. Such a two-moment or two-category scheme would bring the model considerably closer to the warm-rain microphysics used in atmospheric cloud models, while retaining the controlled Rayleigh–Bénard setting.

Beyond the microphysics, several further directions follow naturally. The present simulations are two-dimensional; extending them to three dimensions would allow the fully three-dimensional turbulent cascade and plume dynamics to be represented, at correspondingly higher computational cost. A systematic exploration of the parameter space—in particular the Damköhler number, which controls the ratio of the convective to the phase-change timescale, and the Rayleigh number—would establish how the latent-heat enhancement of the Nusselt number scales across regimes, and whether the transport follows a modified Nu–Ra scaling law in the presence of phase change. Including the ice phase and the associated additional latent heat of fusion would extend the model toward mixed-phase clouds.

Finally, these extensions are motivated not only by physical completeness but also by practical application. A concrete example is offshore wind energy: above the ocean, moist convection in the marine boundary layer—including the evaporatively driven downdraughts and outflows discussed above—modulates the near-surface wind field that offshore wind farms harvest. Improved understanding of how condensation, evaporation, and the associated latent heating and cooling shape these winds therefore feeds directly into wind-resource assessment and power-production forecasting. Idealised configurations such as the present one, in which the latent contribution can be isolated and quantified in a controlled way, provide a rigorous foundation for building that understanding.

Bibliography

[1] Kerry A. Emanuel. *Atmospheric Convection*. Oxford: Oxford University Press, 1994 (cit. on p. 1).

[2] Leo J. Donner. “Deep Convection and Convective Clouds”. In: *Fast Processes in Large-Scale Atmospheric Models: Progress, Challenges, and Opportunities*. Ed. by Yangang Liu and Pavlos Kollias. Hoboken, NJ: American Geophysical Union, 2023. Chap. 5, pp. 121–140. DOI: `10.1002/9781119529019.ch5` (cit. on p. 1).

[3] Jialin Lin, Taotao Qian, Peter Bechtold, Georg Grell, Guang J. Zhang, Ping Zhu, Saulo R. Freitas, Hannah Barnes, and Jongil Han. “Atmospheric Convection”. In: *Reviews of Geophysics* 60.3 (2022), e2021RG000748. DOI: `10.1029/2021RG000748` (cit. on p. 1).

[4] Jr. Houze Robert A. “Mesoscale Convective Systems”. In: *Reviews of Geophysics* 42.4 (2004), RG4003. DOI: `10.1029/2004RG000150` (cit. on pp. 1, 12).

[5] Brian Mapes, Stefan Tulich, Jialin Lin, and Paquita Zuidema. “The mesoscale convection life cycle: Building block or prototype for large-scale tropical waves?” In: *Dynamics of Atmospheres and Oceans* 42.1 (2006), pp. 3–29. DOI: `10.1016/j.dynatmoce.2006.03.003` (cit. on p. 1).

[6] George Hadley. “Concerning the cause of the general trade-winds”. In: *Philosophical Transactions of the Royal Society* 39.437 (1735), pp. 58–62. DOI: `10.1098/rstl.1735.0014`. URL: `https://doi.org/10.1098/rstl.1735.0014` (cit. on p. 2).

[7] Joanne Simpson, Robert F. Adler, and Gerald R. North. “A proposed Tropical Rainfall Measuring Mission (TRMM) satellite”. In: *Bulletin of the American Meteorological Society* 69.3 (1988), pp. 278–295. DOI: 10.1175/1520-0477(1988)069<0278:APTRMM>2.0.CO;2. URL: https://doi.org/10.1175/1520-0477(1988)069%3C0278:APTRMM%3E2.0.CO;2 (cit. on p. 2).

[8] Gilbert T. Walker. “Correlation in seasonal variations of weather. VIII: A preliminary study of world weather”. In: *Memoirs of the India Meteorological Department* 24 (1923), pp. 75–131 (cit. on p. 2).

[9] Jacob Bjerknes. “Atmospheric teleconnections from the equatorial Pacific”. In: *Monthly Weather Review* 97.3 (1969), pp. 163–172. DOI: 10.1175/1520-0493(1969)097<0163:ATFTEP>2.3.CO;2. URL: https://doi.org/10.1175/1520-0493(1969)097%3C0163:ATFTEP%3E2.3.CO;2 (cit. on p. 2).

[10] Roland A. Madden and Paul R. Julian. “Detection of a 40–50 day oscillation in the zonal wind in the tropical Pacific”. In: *Journal of the Atmospheric Sciences* 28.5 (1971), pp. 702–708. DOI: 10.1175/1520-0469(1971)028<0702:DOADOI>2.0.CO;2. URL: https://doi.org/10.1175/1520-0469(1971)028%3C0702:DOADOI%3E2.0.CO;2 (cit. on p. 2).

[11] Herbert Riehl. “A model of hurricane formation”. In: *Journal of Applied Physics* 21.9 (1950), pp. 917–925. DOI: 10.1063/1.1699784. URL: https://doi.org/10.1063/1.1699784 (cit. on p. 2).

[12] J.-L. Lin, Tianjun Qian, and Tomoaki Shinoda. “Stratocumulus clouds in southeastern Pacific simulated by eight CMIP5 CFMIP global climate models”. In: *Journal of Climate* 27.8 (2014), pp. 3000–3022. DOI: 10.1175/JCLI-D-13-00376.1. URL: https://doi.org/10.1175/JCLI-D-13-00376.1 (cit. on p. 2).

[13] Ann Slingo. “Sensitivity of the Earth’s radiation budget to changes in low clouds”. In: *Nature* 343 (1990), pp. 49–51. DOI: 10.1038/343049a0. URL: https://doi.org/10.1038/343049a0 (cit. on p. 2).

[14] J.-L. Lin. “The double-ITCZ problem in IPCC AR4 coupled GCMs: Ocean-atmosphere feedback analysis”. In: *Journal of Climate* 20.18 (2007), pp. 4497–4525. DOI: 10.1175/JCLI4272.1. URL: https://doi.org/10.1175/JCLI4272.1 (cit. on p. 2).

[15] John M. Wallace. “Effect of deep convection on the regulation of tropical sea surface temperature”. In: *Nature* 357 (1992), pp. 230–231. DOI: 10.1038/357230a0. URL: https://doi.org/10.1038/357230a0 (cit. on p. 2).

[16] Linden T. Gidel. “Cumulus cloud transport of transient tracers”. In: *Journal of Geophysical Research: Oceans* 88.C11 (1983), pp. 6587–6599. DOI: 10.1029/JC088iC11p06587. URL: https://doi.org/10.1029/JC088iC11p06587 (cit. on p. 2).

[17] Anne M. Thompson, Wei-Kuo Tao, Kenneth E. Pickering, John R. Scala, and Joanne Simpson. “Tropical deep convection and ozone formation”. In: *Bulletin of the American Meteorological Society* 78.6 (1997), pp. 1043–1054. DOI: 10.1175/1520-0477(1997)078<1043:TDCAOF>2.0.CO;2. URL: https://doi.org/10.1175/1520-0477(1997)078%3C1043:TDCAOF%3E2.0.CO;2 (cit. on p. 2).

[18] Sandrine Bony et al. “Clouds, circulation and climate sensitivity”. In: *Nature Geoscience* 8 (2015), pp. 261–268. DOI: 10.1038/ngeo2398. URL: https://doi.org/10.1038/ngeo2398 (cit. on p. 2).

[19] Bjorn Stevens. “Atmospheric Moist Convection”. In: *Annual Review of Earth and Planetary Sciences* 33 (2005), pp. 605–643. DOI: 10.1146/annurev.earth.33.092203.122658 (cit. on pp. 2–4, 9).

[20] Benjamin M. Sanderson, Karen M. Shell, and William Ingram. “Climate feedbacks determined using radiative kernels in a multi-thousand member ensemble of AOGCMs”. In: *Climate Dynamics* 35 (2010), pp. 1219–1236. DOI: 10.1007/s00382-009-0661-1. URL: https://doi.org/10.1007/s00382-009-0661-1 (cit. on p. 2).

[21] Steven C. Sherwood, Sandrine Bony, and Jean-Louis Dufresne. “Spread in model climate sensitivity traced to atmospheric convective mixing”. In: *Nature* 505 (2014), pp. 37–42. DOI: 10.1038/nature12829. URL: https://doi.org/10.1038/nature12829 (cit. on p. 2).

[22] David A. Stainforth et al. “Uncertainty in predictions of the climate response to rising levels of greenhouse gases”. In: *Nature* 433.7024 (2005), pp. 403–406. DOI: 10.1038/nature03301. URL: https://doi.org/10.1038/nature03301 (cit. on p. 2).

[23] Ming Zhao. “An investigation of the connections among convection, clouds, and climate sensitivity in a global climate model”. In: *Journal of Climate* 27.5 (2014), pp. 1845–1862. DOI: 10.1175/JCLI-D-13-00145.1. URL: https://doi.org/10.1175/JCLI-D-13-00145.1 (cit. on p. 2).

[24] Leo J. Donner. “Progress in Understanding and Parameterizing Fast Physics in Large-Scale Atmospheric Models”. In: *Fast Processes in Large-Scale Atmospheric Models: Progress, Challenges, and Opportunities*. Ed. by Yangang Liu and Pavlos Kollias. Hoboken, NJ: American Geophysical Union, 2023. Chap. 1, pp. 1–13. DOI: 10.1002/9781119529019.ch5 (cit. on p. 2).

[25] D. Kim et al. “Application of MJO Simulation Diagnostics to Climate Models”. In: *Journal of Climate* 22.23 (2009), pp. 6413–6436. DOI: 10.1175/2009JCLI3063.1 (cit. on p. 2).

[26] Katherine H. Straub, Patrick T. Haertel, and George N. Kiladis. “An Analysis of Convectively Coupled Kelvin Waves in 20 WCRP CMIP3 Global Coupled Climate Models”. In: *Journal of Climate* 23.11 (2010), pp. 3031–3056. DOI: 10.1175/2009JCLI3422.1 (cit. on p. 2).

[27] Geoffrey K. Vallis. *Atmospheric and Oceanic Fluid Dynamics*. 2nd ed. Cambridge, UK: Cambridge University Press, 2017 (cit. on pp. 4, 32).

[28] F. Chillà and J. Schumacher. “New Perspectives in Turbulent Rayleigh–Bénard Convectionss”. In: *The European Physical Journal E* 35.7 (2012), p. 58. DOI: 10.1140/epje/i2012-12058-1 (cit. on p. 5).

[29] J. P. Espy. *The Philosophy of Storms*. Boston: Little and Brown, 1841 (cit. on pp. 5, 11).

[30] Grant W. Petty. *A First Course in Atmospheric Thermodynamics*. 1st ed. Madison, Wisconsin: Sundog Publishing, 2008. ISBN: 9780972903321 (cit. on p. 6).

[31] Geoffrey K. Vallis, David J. Parker, and Steven M. Tobias. “A simple system for moist convection: the Rainy–Bénard model”. In: *Journal of Fluid Mechanics* 862 (2019), pp. 162–199. DOI: 10.1017/jfm.2018.872 (cit. on pp. 6, 10, 12, 15–19, 21, 22, 29, 32).

[32] R. R. Rogers and M. K. Yau. *A Short Course in Cloud Physics*. 3rd. Vol. 113. International Series in Natural Philosophy. Oxford: Butterworth-Heinemann, 1989 (cit. on pp. 7, 14, 15).

[33] David Bolton. “The Computation of Equivalent Potential Temperature”. In: *Monthly Weather Review* 108.7 (1980), pp. 1046–1053. DOI: 10.1175/1520-0493(1980)108<1046:TCOEPT>2.0.CO;2 (cit. on p. 8).

[34] Ulrike Lohmann, Felix Lüönd, and Fabian Mahrt. *An Introduction to Clouds: From the Microscale to Climate*. Cambridge: Cambridge University Press, 2016. ISBN: 9781107018228 (cit. on p. 8).

[35] F. H. Busse. “Differential Rotation in Stellar Convection Zones”. In: *The Astrophysical Journal* 159 (Feb. 1970), pp. 629–639. DOI: 10.1086/150337 (cit. on p. 9).

[36] R. J. Bray, R. E. Loughhead, and C. J. Durrant. *The Solar Granulation*. 2nd ed. Cambridge University Press, 1974. ISBN: 978-0-521-11551-3 (cit. on p. 9).

[37] John C. Wyngaard. “Atmospheric Turbulence”. In: *Annual Review of Fluid Mechanics* 24 (1992), pp. 205–234. DOI: 10.1146/annurev.fl.24.010192.001225 (cit. on p. 9).

[38] S. A. Thorpe. “Recent developments in the study of ocean turbulence”. In: *Annual Review of Earth and Planetary Sciences* 32 (2004), pp. 91–109. DOI: 10.1146/annurev.earth.32.071603.152635 (cit. on p. 9).

[39] Rolf Cieszelski. “A Case Study of Rayleigh–Bénard Convection with Clouds”. In: *Beiträge zur Physik der Atmosphäre* 71.2 (1998), pp. 193–210 (cit. on p. 9).

[40] Christiane Normand, Yves Pomeau, and Manuel G. Velarde. “Convective instability: A physicist’s approach”. In: *Reviews of Modern Physics* 49.3 (1977), pp. 581–624. DOI: 10.1103/RevModPhys.49.581 (cit. on p. 9).

[41] Barry A. Klinger and John Marshall. “Regimes and scaling laws for rotating deep convection in the ocean”. In: *Dynamics of Atmospheres and Oceans* 21.3–4 (1995), pp. 227–256. DOI: 10.1016/0377-0265(94)00026-K (cit. on p. 10).

[42] B. W. Atkinson and J. Wu Zhang. “Mesoscale shallow convection in the atmosphere”. In: *Reviews of Geophysics* 34.4 (1996), pp. 403–431. DOI: 10.1029/96RG02623 (cit. on p. 10).

[43] Eric D. Siggia. “High Rayleigh number convection”. In: *Annual Review of Fluid Mechanics* 26 (1994), pp. 137–168. DOI: `10.1146/annurev.fl.26.010194.001033`. URL: `https://doi.org/10.1146/annurev.fl.26.010194.001033` (cit. on p. 10).

[44] Q. Wang, H.-R. Liu, R. Verzicco, O. Shishkina, and D. Lohse. “Regime transitions in thermally driven high-Rayleigh number vertical convection”. In: *Journal of Fluid Mechanics* 917 (2021), A6. DOI: `10.1017/jfm.2021.262`. URL: `https://doi.org/10.1017/jfm.2021.262` (cit. on p. 10).

[45] Kerry A. Emanuel, J. David Neelin, and Christopher S. Bretherton. “On large-scale circulations in convecting atmospheres”. In: *Quarterly Journal of the Royal Meteorological Society* 120 (1994), pp. 1111–1143. URL: `https://api.semanticscholar.org/CorpusID:120732536` (cit. on pp. 10, 14, 16, 18).

[46] Eberhard Bodenschatz, Szymon P. Malinowski, Raymond A. Shaw, and Frank Stratmann. “Can we understand clouds without turbulence?” In: *Science* 327.5968 (2010), pp. 970–971. DOI: `10.1126/science.1181758`. URL: `https://doi.org/10.1126/science.1181758` (cit. on p. 10).

[47] Kamal K. Chandrakar, William Cantrell, Kai Chang, Daniel Ciochetto, Dominik Niedermeier, Mikhail Ovchinnikov, Raymond A. Shaw, and Fan Yang. “Aerosol indirect effect from turbulence-induced broadening of cloud-droplet size distributions”. In: *Proceedings of the National Academy of Sciences of the United States of America* 113.50 (2016), pp. 14243–14248. DOI: `10.1073/pnas.1612686113`. URL: `https://doi.org/10.1073/pnas.1612686113` (cit. on p. 10).

[48] Gabriel Hernandez-Duenas, Andrew J. Majda, Leslie M. Smith, and Samuel N. Stechmann. “Minimal models for precipitating turbulent convection”. In: *Journal of Fluid Mechanics* 717 (2013), pp. 576–611. DOI: `10.1017/jfm.2012.586` (cit. on pp. 12, 13, 15, 16, 21, 22, 28, 29).

[49] Lu Zhang, Kai Leong Chong, and Ke-Qing Xia. “Moisture transfer by turbulent natural convection”. In: *Journal of Fluid Mechanics* 874 (2019), pp. 1041–1056. DOI: `10.1017/jfm.2019.463` (cit. on pp. 12, 15, 16, 19–21, 37).

[50] Subin Thomas, Prasanth Prabhakaran, Fan Yang, Will H. Cantrell, and Raymond A. Shaw. “Dimensionless parameters for cloudy Rayleigh-Bénard convection: Supersaturation, Damköhler, and Nusselt numbers”. In: *Physical Review Fluids* 7 (2022), p. 010503. DOI: `10.1103/PhysRevFluids.7.010503` (cit. on pp. 12, 15, 16, 20–22, 28, 29, 35, 38, 48).

[51] Wojciech W. Grabowski, Xiaoqing Wu, and Mitchell W. Moncrieff. “Cloud Resolving Modeling of Tropical Cloud Systems during Phase III of GATE. Part III: Effects of Cloud Microphysics”. In: *Journal of the Atmospheric Sciences* 56.14 (1999), pp. 2384–2402. DOI: `10.1175/1520-0469(1999)056<2384:CRMOTC>2.0.CO;2` (cit. on p. 12).

[52] Jean-Pierre Lafore and Mitchell W. Moncrieff. “A numerical investigation of the organization and interaction of the convective and stratiform regions of tropical squall lines”. In: *Journal of the Atmospheric Sciences* 46.4 (1989), pp. 521–544. DOI: `10.1175/1520-0469(1989)046<0521:ANIOTO>2.0.CO;2` (cit. on p. 12).

[53] Wojciech W. Grabowski, Xiaoqing Wu, and Mitchell W. Moncrieff. “Cloud-resolving modeling of tropical cloud systems during Phase III of GATE. Part I: Two-dimensional experiments”. In: *Journal of the Atmospheric Sciences* 53.24 (1996), pp. 3684–3709. DOI: `10.1175/1520-0469(1996)053<3684:CRMOTC>2.0.CO;2` (cit. on p. 12).

[54] Kuan-Man Xu and David A. Randall. “Explicit simulation of cumulus ensembles with the GATE Phase III data: Comparison with observations”. In: *Journal of the Atmospheric Sciences* 53.24 (1996), pp. 3710–3736. DOI: `10.1175/1520-0469(1996)053<3710:ESOCEW>2.0.CO;2` (cit. on p. 12).

[55] Christopher Lucas, Edward J. Zipser, and Bradley S. Ferrier. “Sensitivity of tropical west Pacific oceanic squall lines to tropospheric wind and moisture profiles”. In: *Journal of the Atmospheric Sciences* 57.15 (2000), pp. 2351–2373. DOI: `10.1175/1520-0469(2000)057<2351:SOTWPO>2.0.CO;2` (cit. on p. 12).

[56] Chun Liu and Mitchell W. Moncrieff. “Cumulus ensembles in shear: Implications for parameterization”. In: *Journal of the Atmospheric Sciences* 58.18 (2001), pp. 2832–2842. DOI: `10.1175/1520-0469(2001)058<2832:CEISIF>2.0.CO;2` (cit. on p. 12).

[57] Yoshimitsu Ogura and Norman A. Phillips. “Scale analysis of deep and shallow convection in the atmosphere”. In: *Journal of the Atmospheric Sciences* 19.2 (1962), pp. 173–179. DOI: `10.1175/1520-0469(1962)019<0173:SAODAS>2.0.CO;2` (cit. on pp. 12, 13).

[58] Francis B. Lipps and Robert S. Hemler. “A scale analysis of deep moist convection and some related numerical calculations”. In: *Journal of the Atmospheric Sciences* 39.10 (1982), pp. 2192–2210. DOI: `10.1175/1520-0469(1982)039<2192:ASAODM>2.0.CO;2` (cit. on pp. 12, 13).

[59] Peter R. Bannon. “On the anelastic approximation for a compressible atmosphere”. In: *Journal of the Atmospheric Sciences* 53.24 (1996), pp. 3618–3628. DOI: `10.1175/1520-0469(1996)053<3618:OTAAFA>2.0.CO;2` (cit. on pp. 12, 13).

[60] Geoffrey K. Vallis. *Atmospheric and Oceanic Fluid Dynamics: Fundamentals and Large-Scale Circulation*. Cambridge: Cambridge University Press, 2006. ISBN: 9780521849692 (cit. on pp. 12, 13, 15).

[61] E. Kessler. *On the Distribution and Continuity of Water Substance in Atmospheric Circulations*. Vol. 32. Meteorological Monographs. American Meteorological Society, 1969 (cit. on pp. 14, 47).

[62] Wojciech W. Grabowski and Terry L. Clark. "Cloud–environment interface instability, Part II: Extension to three spatial dimensions". In: *Journal of the Atmospheric Sciences* 50.4 (1993), pp. 555–573. DOI: 10.1175/1520-0469(1993)050<0555:CEIIPE>2.0.CO;2 (cit. on p. 14).

[63] H. L. Kuo. "Convection in conditionally unstable atmosphere". In: *Tellus* 13.4 (1961), pp. 441–459 (cit. on p. 15).

[64] Christopher S. Bretherton. "A Theory for Nonprecipitating Moist Convection between Two Parallel Plates. Part I: Thermodynamics and Linear Solutions". In: *Journal of the Atmospheric Sciences* 44.14 (1987), pp. 1809–1827. DOI: 10.1175/1520-0469(1987)044<1809:ATFNMC>2.0.CO;2 (cit. on pp. 15, 19).

[65] J. W. M. Cuijpers and P. G. Duynkerke. "Large eddy simulation of trade wind cumulus clouds". In: *Journal of the Atmospheric Sciences* 50.23 (1993), pp. 3894–3908 (cit. on p. 15).

[66] B. Stevens. "On the growth of layers of nonprecipitating cumulus convection". In: *Journal of the Atmospheric Sciences* 64 (2007), pp. 2916–2931 (cit. on p. 15).

[67] Keith L. Seitter and Hsiao-Lan Kuo. "The dynamical structure of squall-line type thunderstorms". In: *Journal of the Atmospheric Sciences* 40.12 (1983), pp. 2831–2854. DOI: 10.1175/1520-0469(1983)040<2831:TDSOSL>2.0.CO;2 (cit. on p. 15).

[68] Kerry A. Emanuel. "Some dynamical aspects of precipitating convection". In: *Journal of the Atmospheric Sciences* 43.20 (1986), pp. 2183–2198. DOI: 10.1175/1520-0469(1986)043<2183:SDAOPC>2.0.CO;2 (cit. on p. 15).

[69] Andrew J. Majda and Y. Xing. "New multi-scale models on mesoscales and squall lines". In: *Communications in Mathematical Sciences* 8.1 (2010), pp. 113–144. DOI: 10.4310/CMS.2010.v8.n1.a6 (cit. on p. 15).

[70] Jai Sukhatme, Andrew J. Majda, and Leslie M. Smith. "Two-dimensional moist stratified turbulence and the emergence of vertically sheared horizontal flows". In: *Physics of Fluids* 24.3 (2012), p. 036602. DOI: 10.1063/1.3697697 (cit. on p. 15).

[71] Qiang Deng, Leslie M. Smith, and Andrew J. Majda. "Tropical cyclogenesis and vertical shear in a moist Boussinesq model". In: *Journal of Fluid Mechanics* 706 (2012), pp. 384–412. DOI: 10.1017/jfm.2012.297 (cit. on p. 15).

[72] Hadi Zanganeh Kia, Fan Yang, Marat Khairoutdinov, Raymond A. Shaw, Aaron Wang, and Yunsco Choi. "Exploring the impact of surface topography on Rayleigh–Bénard dry convection in the Pi cloud chamber using OpenFOAM: In cylindrical and rectangular geometries". In: *Atmospheric Research* 323 (2025), p. 108144. DOI: 10.1016/j.atmosres.2025.108144 (cit. on pp. 16, 17).

[73] Guenter Ahlers, Siegfried Grossmann, and Detlef Lohse. "Heat transfer and large-scale dynamics in turbulent Rayleigh–Bénard convection". In: *Reviews of Modern Physics* 81.2 (2009), pp. 503–537. DOI: 10.1103/RevModPhys.81.503 (cit. on pp. 17, 18, 35).

[74] François Chillà and Jörg Schumacher. "New perspectives in turbulent Rayleigh–Bénard convection". In: *The European Physical Journal E* 35.7 (2012), p. 58. DOI: 10.1140/epje/i2012-12058-1 (cit. on pp. 17, 18).

[75] Alessandro Parodi, Kerry A. Emanuel, and Antonello Provenzale. "Plume patterns in radiative–convective flows". In: *New Journal of Physics* 5.1 (2003), p. 106. DOI: 10.1088/1367-2630/5/1/106 (cit. on p. 17).

[76] Marco Berlengiero, Kerry A. Emanuel, Jost von Hardenberg, Antonello Provenzale, and Edward A. Spiegel. "Internally cooled convection: A fillip for Philip". In: *Communications in Nonlinear Science and Numerical Simulation* 17.5 (2012), pp. 1998–2007. DOI: 10.1016/j.cnsns.2011.10.021 (cit. on p. 17).

[77] Andrei S. Monin and Alexander M. Obukhov. "Basic laws of turbulent mixing in the surface layer of the atmosphere". In: *Trudy Geofizicheskogo Instituta AN SSSR* 24 (1954), pp. 163–187 (cit. on p. 17).

[78] Richard S. Scorer and Frank H. Ludlam. "Bubble theory of penetrative convection". In: *Quarterly Journal of the Royal Meteorological Society* 79.339 (1953), pp. 94–103. DOI: 10.1002/qj.49707933908 (cit. on p. 18).

[79] Bruce R. Morton, G. I. Taylor, and John S. Turner. "Turbulent gravitational convection from maintained and instantaneous sources". In: *Proceedings of the Royal Society of London A* 234.1196 (1956), pp. 1–23. DOI: 10.1098/rspa.1956.0011 (cit. on p. 18).

[80] Frank H. Ludlam. "Cumulus and cumulonimbus convection". In: *Tellus* 18.3 (1966), pp. 687–698. DOI: 10.1111/j.2153-3490.1966.tb00274.x (cit. on p. 18).

[81] George H. Bryan, John C. Wyngaard, and J. M. Fritsch. "Resolution requirements for the simulation of deep moist convection". In: *Monthly Weather Review* 131.10 (2003), pp. 2394–2416. DOI: 10.1175/1520-0493(2003)131<2394:RRFTSO>2.0.CO;2 (cit. on p. 18).

[82] Joseph Smagorinsky. "General circulation experiments with the primitive equations. Part I. The basic experiment". In: *Monthly Weather Review* 91.3 (1963), pp. 99–164. DOI: 10.1175/1520-0493(1963)091<0099:GCEWTP>2.3.CO;2 (cit. on p. 18).

[83] George L. Mellor and Tetsuji Yamada. "A hierarchy of turbulence closure models for planetary boundary layers". In: *Journal of the Atmospheric Sciences* 31.7 (1974), pp. 1791–1806. DOI: 10.1175/1520-0469(1974)031<1791:AHOTCM>2.0.CO;2 (cit. on p. 18).

[84] Siegfried Grossmann and Detlef Lohse. “Scaling in thermal convection: A unifying theory”. In: *Journal of Fluid Mechanics* 407 (2000), pp. 27–56. DOI: 10.1017/S0022112099007545 (cit. on p. 18).

[85] Christopher S. Bretherton. “A Theory for Nonprecipitating Convection between Two Parallel Plates. Part II: Nonlinear Theory and Cloud Field Organization”. In: *Journal of the Atmospheric Sciences* 45.17 (1988), pp. 2391–2415. DOI: 10.1175/1520-0469(1988)045<2391:ATFNMC>2.0.CO;2 (cit. on p. 19).

[86] Kim Spyksma, Peter Bartello, and M. K. Yau. “A Boussinesq moist turbulence model”. In: *Journal of Turbulence* 7 (2006), N32. DOI: 10.1080/14685240600688688 (cit. on p. 19).

[87] Olivier Pauluis and Jörg Schumacher. “Idealized moist Rayleigh–Bénard convection with piecewise linear equation of state”. In: *Communications in Mathematical Sciences* 8.1 (2010), pp. 295–319. DOI: 10.4310/CMS.2010.v8.n1.a13 (cit. on p. 19).

[88] Jörg Schumacher and Olivier Pauluis. “Buoyancy statistics in moist turbulent Rayleigh–Bénard convection”. In: *Journal of Fluid Mechanics* 648 (2010), pp. 509–519. DOI: 10.1017/S0022112009993683 (cit. on p. 19).

[89] L. E. Schmidt, P. Oresta, F. Toschi, R. Verzicco, D. Lohse, and A. Prosperetti. “Modification of turbulence in Rayleigh–Bénard convection by phase change”. In: *New Journal of Physics* 13.2 (2011), p. 025002. DOI: 10.1088/1367-2630/13/2/025002 (cit. on p. 19).

[90] R. Lakkaraju, Richard J. A. M. Stevens, P. Oresta, R. Verzicco, D. Lohse, and A. Prosperetti. “Heat transport in bubbling turbulent convection”. In: *Proceedings of the National Academy of Sciences* 110.23 (2013), pp. 9237–9242. DOI: 10.1073/pnas.1301935110 (cit. on p. 19).

[91] Ulrich R. Christensen. “Effects of phase transitions on mantle convection”. In: *Annual Review of Earth and Planetary Sciences* 23.1 (1995), pp. 65–87. DOI: 10.1146/annurev.ea.23.050195.000433 (cit. on p. 19).

[92] P. A. Mangarella, A. J. Chambers, Robert L. Street, and E. Y. Hsu. “Laboratory studies of evaporation and energy transfer through a wavy air–water interface”. In: *Journal of Physical Oceanography* 3.1 (1973), pp. 93–101. DOI: 10.1175/1520-0485(1973)003<0093:LSOEAE>2.0.CO;2 (cit. on p. 22).

[93] Raymond A. Shaw. “Particle-Turbulence Interactions in Atmospheric Clouds”. In: *Annual Review of Fluid Mechanics* 35 (2003), pp. 183–227. DOI: 10.1146/annurev.fluid.35.101101.161125 (cit. on p. 23).

[94] Gaetano Sardina, Francesco Picano, Luca Brandt, and Rodrigo Caballero. “Continuous Growth of Droplet Size Variance due to Condensation in Turbulent Clouds”. In: *Physical Review Letters* 115.18 (2015), p. 184501. DOI: 10.1103/PhysRevLett.115.184501 (cit. on p. 23).

[95] Alessandra S. Lanotte, Agnese Seminara, and Federico Toschi. "Cloud Droplet Growth by Condensation in Homogeneous Isotropic Turbulence". In: *Journal of the Atmospheric Sciences* 66.6 (2009), pp. 1685–1697. DOI: 10.1175/2008JAS2736.1 (cit. on p. 23).

[96] Gaetano Sardina, Stéphane Poulain, Luca Brandt, and Rodrigo Caballero. "Broadening of Cloud Droplet Size Spectra by Stochastic Condensation: Effects of Mean Updraft Velocity and CCN Activation". In: *Journal of the Atmospheric Sciences* 75.2 (2018), pp. 451–467. DOI: 10.1175/JAS-D-17-0241.1 (cit. on p. 23).

[97] M. R. Baer and J. W. Nunziato. "A two-phase mixture theory for the deflagration-to-detonation transition (DDT) in reactive granular materials". In: *International Journal of Multiphase Flow* 12.6 (1986), pp. 861–889. DOI: 10.1016/0301-9322(86)90033-9 (cit. on pp. 23, 24).

[98] R. Saurel and R. Abgrall. "A multiphase Godunov method for compressible multifluid and multiphase flows". In: *Journal of Computational Physics* 150.2 (1999), pp. 425–467 (cit. on p. 24).

[99] Lionel Sainsaulieu. "Euler System Modeling Vaporizing Sprays". In: *Journal of Propulsion and Power* 8.2 (1992), pp. 280–287. DOI: 10.2514/3.23586 (cit. on p. 24).

[100] Salar Zamani Salimi, Aritra Mukherjee, Marica Pelanti, and Luca Brandt. "A low Mach number diffuse-interface model for multicomponent two-phase flows with phase change". In: *Journal of Computational Physics* 523 (2025), p. 113683. ISSN: 0021-9991. DOI: https://doi.org/10.1016/j.jcp.2024.113683. URL: https://www.sciencedirect.com/science/article/pii/S0021999124009318 (cit. on pp. 26, 27, 31).

[101] Dan Li. "Turbulent Prandtl number in the atmospheric boundary layer: Where are we now?" In: *Atmospheric Research* 216 (2019), pp. 86–105. ISSN: 0169-8095. DOI: 10.1016/j.atmosres.2018.09.015 (cit. on p. 35).

[102] Yoshihide Tominaga and Ted Stathopoulos. "Turbulent Schmidt numbers for CFD analysis with various types of flowfield". In: *Atmospheric Environment* 41.37 (2007), pp. 8091–8099. ISSN: 1352-2310. DOI: 10.1016/j.atmosenv.2007.06.054 (cit. on p. 35).

[103] T. K. Flesch, J. H. Prueger, and J. L. Hatfield. "Turbulent Schmidt number from a tracer experiment". In: *Agricultural and Forest Meteorology* 111.4 (2002), pp. 299–307. DOI: 10.1016/S0168-1923(02)00025-4 (cit. on p. 35).

[104] Olga Shishkina, Richard J. A. M. Stevens, Siegfried Grossmann, and Detlef Lohse. "Boundary layer structure in turbulent thermal convection and its consequences for the required numerical resolution". In: *New J. Phys.* 12 (2010), p. 075022 (cit. on p. 35).

Dedications

To my mother, my father, and my brother.